Journal of Environmental Chemical Engineering 13 (2025) 118641

Contents lists available at ScienceDirect

Journal of Environmental Chemical Engineering

journal homepage: www.elsevier.com/locate/jece

Influence of synthesis variables on the physicochemical properties of lignin-derived cryogels for levulinic acid production from oil palm mesocarp fiber

Nadiah Syafiqah Mohd Azlan [a], Chiew Lin Yap [a,*], Yong Wei Tiong [b], Suyin Gan [a], Mohd Basyaruddin Abdul Rahman [c]

[a] Faculty of Science and Engineering, University of Nottingham Malaysia, Jalan Broga, Semenyih, 43500 Selangor, Malaysia
[b] Institute of Sustainability for Chemicals, Energy and Environment (ISCE2), Agency for Science, Technology and Research (A*STAR), 1 Pesek Road, Jurong Island, Singapore 6278333, Republic of Singapore
[c] Department of Chemistry, Faculty of Science, Universiti Putra Malaysia, 43400 UPM Serdang, Selangor, Malaysia

ARTICLE INFO

Keywords:
Carbon cryogel
Levulinic acid
Microwave conversion
Response surface methodology
Synergistic effect

ABSTRACT

In an era where sustainable biomass conversion is paramount, this research investigates the impact of preparation conditions of $H_3PW_{12}O_{40}$-Nb_2O_5 supported carbon cryogels on levulinic acid (LA) production via microwave-assisted conversion of oil palm mesocarp fiber. These cryogels offer an energy-efficient, eco-friendly alternative to traditional mineral acid catalysts, forming LA under mild conditions (2 min, <180 °C). The study examines how preparation parameters, including the Brønsted to Lewis acid ratio, calcination, and solvent exchange, influence cryogel properties and LA yield. A maximum LA yield of 20.1 % was achieved, with the optimized cryogel exhibiting a surface area of 57.41 $m^2\ g^{-1}$, porosity of 0.13 $cm^3\ g^{-1}$, and medium acid sites of 7.45 mmol g^{-1} . The balanced distribution of micropores, mesopores, and macropores facilitated larger biomass particle passage, enhancing thermal conductivity and uniform heat transfer. The interplay of Brønsted-Lowry and Lewis acidity (ratio 1.48) fostered a synergistic effect in catalyzing tandem reaction steps, achieving a synergy factor of 2.15. This work highlights the potential of lignin-derived carbon cryogels in revolutionizing fast, safe, and clean biomass conversion to LA, achieving a one-pot conversion efficiency of 88.5 %. Optimizing preparation parameters enhances catalyst properties, improving LA production efficiency and yield.

1. Introduction

Over the past decade, interest in lignocellulosic biomass has grown significantly, particularly for the production of platform chemicals such as levulinic acid (LA). LA is a highly reactive keto acid, featuring both carboxylic acid (–COOH) and ketone (–C═O) groups, which makes it a versatile precursor for a wide range of value-added products, including diphenolic acid, γ-valerolactone, LA esters, and amino derivatives [1]. These compounds find applications across diverse industries, including pharmaceuticals, biofuels and agrochemicals [2].

Traditionally, LA is produced through petrochemical processes involving the hydrolysis and hydrogenation of maleic anhydride or furfuryl alcohol [1]. However, such routes are often complex and costly, contributing to a high market price of approximately US$10/kg [3]. In light of sustainability concerns, recent efforts have focused on producing LA from renewable biomass residues. Despite promising advances, the commercialization of biomass-based LA remains in its early stages [4], [5], [6].

Lignocellulosic biomass—comprising cellulose (35–55 wt%), hemicellulose (25–35 wt%), and lignin (15–30 wt%)—serves as a promising feedstock for LA production [4], [5] [7], [8]. Common sources include sugarcane bagasse and oil palm biomass [9], [10], [11], [12], with the latter being particularly abundant in Malaysia (approximately 83 million dry tons annually [13]). However, its potential for conversion into high-value chemicals like LA remains underutilized, underscoring the need for improved biomass valorization strategies.

Catalysts play a crucial role in converting cellulose to LA. While homogeneous Brønsted acids such as sulfuric and hydrochloric acid are effective [14], [15], their corrosiveness and downstream recovery issues can lead to LA degradation into gaseous byproducts like hydrogen (H_2),

* Corresponding author.
E-mail address: Chiew-Lin.Yap@nottingham.edu.my (C.L. Yap).

https://doi.org/10.1016/j.jece.2025.118641
Received 1 May 2025; Received in revised form 29 July 2025; Accepted 11 August 2025
Available online 12 August 2025

methane (CH_4), and carbon monoxide (CO) [16]. This has driven interest in heterogeneous catalysts, which offer better recyclability and process stability [17], [18], [19], [20]. Among these, sulfonated carbon-based solid acids are attractive due to their high acid site density and economic feasibility [21], [22], [23], although their synthesis often requires high-temperature treatments (>500 °C) to enhance performance and stability [24], [25], [26].

Lignin, the second most abundant natural biopolymer after cellulose, is rich in carbon and aromatic functionalities, making it a valuable precursor for carbon-based solid catalysts [21]. While activated carbon derived from lignin offers high surface area and reactivity [22], its production is energy-intensive. As a milder alternative, lignin-derived cryogels prepared via sol-gel methods at 70–180 °C have emerged as promising catalyst supports. These cryogels feature a three-dimensional porous architecture suitable for accommodating a range of reactant sizes [23], [24]. Nonetheless, to enhance their activity and selectivity for LA production, incorporation of additional acid functionalities is required.

Among acid catalysts, polyoxometalates (heteropoly acids) — notably $H_3PW_{12}O_{40}$ and $H_4SiW_{12}O_{40}$ — exhibit superacidity, surpassing even conventional mineral acids like H_2SO_4, HNO_3, and HCl [25]. These heteropolyacids are effective and recyclable in cellulose hydrolysis, although recovery from homogeneous systems often requires an extraction step. Niobium-based catalysts also hold promise, offering thermal stability and abundant Lewis acid sites conducive to tandem steps of biomass conversion [26]. Recent studies indicate that modified niobium catalysts significantly enhance LA selectivity [27], [28]. Moreover, co-deposition of polyoxometalates and niobium oxides onto lignin cryogels introduces both Brønsted and Lewis acid sites, enabling superior catalytic performance, selectivity, and resistance to deactivation [26]. Lignin cryogels incorporated with acid catalysts can be engineered to achieve desirable acidity, pore structure, and aqueous-phase stability, yet studies on their use as catalysts for biomass-to-LA conversion remain limited. To date, only three notable investigations have explored lignin-based solid acid catalysts for cellulose conversion, as summarized in Table 1 [29].

To address this gap, the present study explores lignin-derived carbon cryogels incorporated with phosphotungstic acid ($H_3PW_{12}O_{40}$) and niobium(V) oxide (Nb_2O_5) for catalytic conversion of biomass to LA. These bifunctional catalysts leverage synergistic Brønsted-Lewis acid interactions to promote key reaction pathways, including cellulose hydrolysis, glucose isomerization, and hydroxymethylfurfural (HMF) rehydration [27] [28], [31], [32]. For example, mesoporous niobium-based catalysts have been shown to achieve high LA yields under aqueous conditions at 180 °C over 24 h [33], [34]. Additionally, this study employs a microwave-assisted method to further enhance catalytic efficiency. Microwave irradiation delivers rapid and uniform energy transfer, accelerating reaction rates and significantly reducing reaction time. Prior work using concentrated $H_3PW_{12}O_{40}$ has achieved glucose yields up to 75.6 % at just 90 °C within 3 h under microwave conditions [35].

While carbon cryogels have been employed in catalysis, lignin-derived variants remain relatively underexplored. A comprehensive understanding of key synthesis parameters—such as the Brønsted-to-Lewis acid ratio, calcination conditions (e.g. temperature and holding time), and solvent exchange method—is crucial, as these factors directly influence critical properties including surface area, porosity, acidity, and functional group composition. These characteristics govern catalyst–biomass interactions and impact LA yield.

To this end, the current study applies a multivariate optimization strategy using Response Surface Methodology (RSM) coupled with Central Composite Design (CCD). This framework enables a systematic evaluation of synthesis parameters and their effects on cryogel physicochemical characteristics and catalytic performance. The integration of $H_3PW_{12}O_{40}$ and Nb_2O_5 into lignin-based cryogels, combined with microwave-assisted conversion, offers a promising and sustainable pathway for LA production from oil palm mesocarp fiber.

2. Materials and methods

2.1. Materials and chemicals

Oil palm mesocarp fiber (OPMF) was obtained as pressed fibrous strands and prepared into dewaxed OPMF following a previously reported method [36]. γ-valerolactone (99 %) and levulinic acid (99 %) were sourced from Sigma Aldrich (Darmstadt, Germany), while *t*-butanol was procured from Thermo Fisher Scientific (Pittsburgh, USA). Phosphotungstic acid ($H_3PW_{12}O_{40}$) and niobium oxide (Nb_2O_5) were obtained from Nacalai Tesque (Kyoto, Japan). Alkaline lignin and xanthan gum were purchased from Tokyo Chemical (Japan). All reagents were of analytical grade and used without further purification. Ultrapure water (18.2 MΩ·cm, <0.01 CFU mL^{-1}, <1 particulate mL^{-1}) was produced using a Milli-Q water purification system from Merck (Darmstadt, Germany).

2.2. Carbon cryogel synthesis

A lignin–xanthan gum (LIG-XG) hydrogel incorporating $H_3PW_{12}O_{40}$ and Nb_2O_5 was synthesized following a previously reported method [37]. $H_3PW_{12}O_{40}$ primarily exhibits Brønsted–Lowry acidity, whereas Nb_2O_5 acts as a Lewis acid. The sol–gel–hydrothermal synthesis procedure is illustrated in Fig. 1. Following synthesis, the hydrogel was rinsed with deionized water to remove unreacted monomers and subsequently immersed in *t*-butanol at ten times its volume (approximately 30 mL) to facilitate solvent exchange with water prior to freeze-drying. The sample was pre-frozen overnight and then freeze-dried at −40 °C for 12 h to obtain a cryogel. Calcination was carried out in a Carbolite Gero ashing furnace (AAF 11/32) at a ramp rate of 5 °C min^{-1}, enabling high volumes of preheated air to circulate through the chamber, thereby enhancing combustion and the removal of volatiles. This thermal treatment was essential for activating the embedded inorganic phases of $H_3PW_{12}O_{40}$ and Nb_2O_5 and for promoting phase transitions that reinforce pore wall rigidity and structural stability.

Table 1
Literature studies on lignin-based catalysts for cellulose conversion to LA.

Ref.	Feedstock	Catalyst	Reaction medium	Characteristics				LA yield (%)
				S_{BET} (m^2 g^{-1})	V_p (cm^3 g^{-1})	d_p (nm)	Acidity (mmol g^{-1})	
[29]	Microcrystalline cellulose	Lignin-based catalyst doped with FeS (impregnation method)	185 °C, 120 min in GVL (monophasic system)	21.61	0.04	4.13	-	35.6
[30]	Cellulose residue	Phosphoric acid-activated lignin-based solid acid catalysts (impregnation method)	190 °C, 150 min in MIBK/H_2O-NaCl (biphasic system	583.1	0.66	4.74	2.81	67.9
[12]	Cellulose from sugarcane	Lignin-based solid acid catalyst	140 °C, 6 h in water (monophasic system)	-	-	1.48	-	38.6

S_{BET}: Surface area based on the *Brunauer–Emmett–Teller* (BET) method, V_p: Pore volume, d_p: Pore diameter

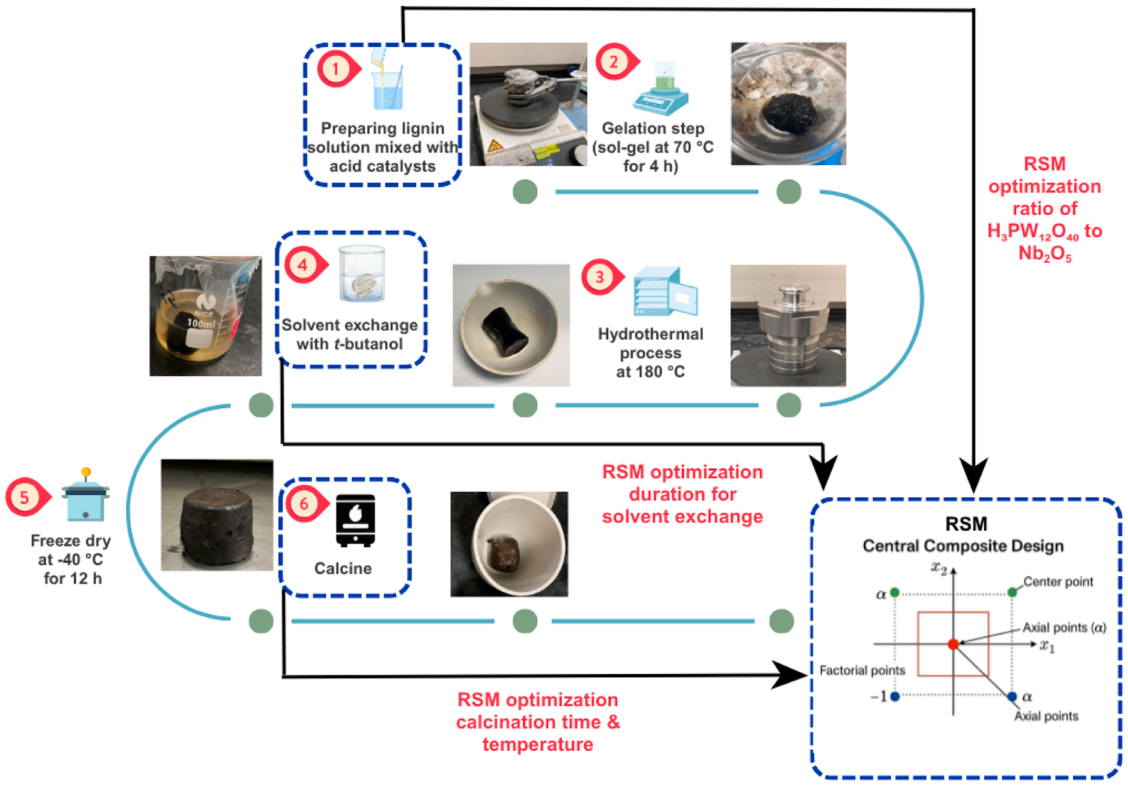

Fig. 1. Synthesis and optimization workflow of lignin-derived carbon cryogel, highlighting variable parameters in Steps 1, 4, and 6 as defined by the RSM experimental design.

2.3. Microwave conversion of biomass to LA

The dewaxed OPMF (0.1 g) was added into a borosilicate reactor containing 5 mL of GVL and 0.5 mL of water. A carbon cryogel catalyst (0.2 g) was added to the reactor. The reaction was carried out via microwave irradiation (SAMSUNG, Model ME711K, 230 V/50 Hz) at 450 W for 2 min. An infrared IR Laser thermometer and a laboratory thermometer were used to determine the temperature of the solvent after the effect of heating. Upon heating, the reaction mixture was quickly quenched with iced water to stop the side reactions. The supernatant of the product sample was extracted from the reactor and measured for its final volume and then diluted in the 100 mL volumetric flask. The sample (1 mL) was filtered through a 0.22 μm PTFE syringe filter into a 2 mL vial, and 0.2 mL of internal standard was injected into the same vial. The sample mixture was vortexed for 1 min and ready for product quantification.

2.4. Product analysis

The LA product was quantified using high-performance liquid chromatography coupled with a variable wavelength detector (HPLC-VWD, Agilent Series 1210, USA). The LA peak in the chromatogram was detected using an Aminex HPX-87H column (BioRad, 300 ×7.8 mm) under isocratic conditions with 5 mM sulfuric acid at 60 °C, a flow rate of 0.6 mL min^{-1}, an injection volume of 20 μL, and detection at λ = 190 nm. Method validation (see Supplementary material) was conducted to assess the precision, linearity, and sensitivity of the analytical method. The final percentage of LA was calculated using Eq. (1), the theoretical maximum yield of LA from cellulose conversion was determined using Eq. (2), and LA efficiency was calculated using Eq. (3).

$$\text{Actual LA yield}(\%) = \frac{\text{Amount of LA}(g)}{\text{Initial biomass loading}(g)} \times 100 \quad (1)$$

$$\text{Theoretical LA yield}(\%) = \frac{\text{Cellulose content in biomass}(g) \times 0.71}{\text{Initial biomass loading}(g)}$$

where

$$\frac{\text{Molecular weight of LA}\left(g\ mol^{-1}\right)}{\text{Molecular weight of cellulose}\left(g\ mol^{-1}\right)} = \frac{116}{162} = 0.71 \quad (2)$$

$$\text{Efficiency of LA}(\%) = \frac{\text{Experimental yield}}{\text{Theoretical yield}} \times 100\% \quad (3)$$

2.5. Response surface methodology

A central composite design (CCD) within response surface methodology (RSM) was employed to optimize carbon cryogels for LA production. Key parameters—including the $H_3PW_{12}O_{40}$:Nb_2O_5 ratio, solvent exchange duration, and calcination conditions—were adapted from established protocols [38], [39], and the experimental layout was devised using Design Expert Version 13. All variables listed in Table 2 were tested at five levels, and optimization trials were validated in

Table 2
Parametric studies: Carbon cryogel attributes.

Factors	Symbol	Levels				
		-∝[a]	-1[b]	0[c]	+ 1[a]	+∝[b]
Calcination temperature (°C)	A	100	200	300	400	500
Calcination time (min)	B	15	30	45	60	75
Ratio of $H_3PW_{12}O_{40}$ to Nb_2O_5	C	1	2	3	4	5
Solvent exchange (h)	D	2	8	14	20	26

[a] –∝ and + ∝: Star points beyond factorial region that help to estimate curvature (quadratic effects) of the response surface
[b] 0: Baseline or middle level of the variable
[c] –1 and + 1: Lower and higher level in the factorial design

triplicate using Eq. (4).

$$\text{Error} = |\text{Validation result} - \text{CCD result}| \,/\, \text{CCD result} \times 100 \quad (4)$$

The study incorporated 16 factorial points, 8 axial points, and 6 center point replicates, yielding 30 total runs. The number of experiments (N) was determined using Eq. (5).

$$N = 2^{n} + 2n + n_c \quad (5)$$

where n is the number of factor and n_c is the number of center point replicates.

To predict optimal conditions, a second-order polynomial model was fitted as shown in Eq. (6).

$$Y = \beta_0 + \sum_{i=1}^{n} \beta_i X_i + \sum_{i=1}^{n} \beta_{ii} X_i^2 + \sum_{i=1}^{n} \sum_{j>1}^{n} \beta_{ij} X_i X_j \quad (6)$$

where Y is the predicted response, β_0, β_i, β_{ii}, β_{ij} are regression coefficients for the constant, linear, quadratic and interaction terms, and, X_i and X_j are the coded independent variables.

Solvent exchange durations ranged from 2 to 26 h, with 24 h commonly reported as optimal for preserving pore structure while enabling effective solvent replacement [39]. Prolonged exposure may lead to structural shrinkage. This step is emphasized as a critical pre-treatment, particularly under inconsistent ambient temperature regulation during freeze-drying, since volatile solvents such as *t*-butanol help lower the freezing point, minimize ice crystal formation, and enhance pore preservation.

The calcination temperature range was selected based on literature findings [40], which report optimal cryogel performance for ethyl levulinate production around 500 °C, with a decline in yield observed above 550 °C. A CCD temperature range of 100–500 °C was selected to span key decomposition events: xanthan gum begins degrading near 250 °C, lignin around 300 °C, and carbon cryogels with metal additives undergo structural transformations between 400–500 °C. This allows a comprehensive evaluation of pore evolution, crystallinity, and sintering effects during thermal treatment.

Model adequacy was assessed using analysis of variance (ANOVA), the coefficient of determination (R^2), and significance testing via Fisher's F-test. A p-value < 0.05 was used to identify significant model terms. Three-dimensional response surface and contour plots were generated to visualize the interactions between variables, and numerical optimization was performed to maximize LA yield under the assumption of equal variance

2.6. Characterization of carbon cryogel

Seven catalyst samples—O1, O8, O11, O15, O21, O22, and OPT2—were selected from the experimental matrix for detailed characterization. These represent key points in the CCD: factorial points (O1, O8, O11, O15), axial points (O21 and O22), and the model-optimized condition (OPT2). Center point replicates were excluded, as their purpose was solely to estimate experimental error and reproducibility, rather than to capture property changes related to synthesis variables. This selection strategy provides broad coverage of the design space, enabling thorough evaluation of how changes in preparation conditions affect catalyst properties and LA yield. Each sample label corresponds to a distinct combination of synthesis parameters, including the ratio of $H_3PW_{12}O_{40}$ to Nb_2O_5, calcination temperature and duration, and solvent exchange period. The full preparation details for each sample are summarized in Table 3, and these labels are used consistently throughout the study for clarity and ease of reference.

FTIR (ATR-FTIR, Perkin Elmer Frontier FT Mid-IR/Far-IR, USA) analysis was performed to observe alterations in the functional groups present in carbon cryogels incorporated with $H_3PW_{12}O_{40}$-Nb_2O_5. Functional groups were identified by comparison with an IR spectrum table.

Table 3
Parametric studies on factors affecting carbon cryogel properties throughout the synthesis process.

Run	Point type	Parameters				Response
		A	B	C	D	Y_i
		Calcination temperature (°C)	Calcination time (min)	Ratio of $H_3PW_{12}O_{40}$ to Nb_2O_5	Solvent exchange time (h)	LA yield (%)
O1	Factorial	200(−1)	30(−1)	2(−1)	8(−1)	12.40
O2	Factorial	400(+1)	30(−1)	2(−1)	8(−1)	15.40
O3	Factorial	200(−1)	60(+1)	2(−1)	8(−1)	13.40
O4	Factorial	400(+1)	60(+1)	2(−1)	8(−1)	17.15
O5	Factorial	200(−1)	30(−1)	4(+1)	8(−1)	11.67
O6	Factorial	400(+1)	30(−1)	4(+1)	8(−1)	15.23
O7	Factorial	200(−1)	60(+1)	4(+1)	8(−1)	13.98
O8	Factorial	400(+1)	60(+1)	4(+1)	8(−1)	16.52
O9	Factorial	200(−1)	30(−1)	2(−1)	20(+1)	11.19
O10	Factorial	400(+1)	30(−1)	2(−1)	20(+1)	13.13
O11	Factorial	200(−1)	60(+1)	2(−1)	20(+1)	9.43
O12	Factorial	400(+1)	60(+1)	2(−1)	20(+1)	11.85
O13	Factorial	200(−1)	30(−1)	4(+1)	20(+1)	13.89
O14	Factorial	400(+1)	30(−1)	4(+1)	20(+1)	16.44
O15	Factorial	200(−1)	60(+1)	4(+1)	20(+1)	12.82
O16	Factorial	400(+1)	60(+1)	4(+1)	20(+1)	14.47
O17	Axial	100(-∝)	45(0)	3(0)	14(0)	9.67
O18	Axial	500(+∝)	45(0)	3(0)	14(0)	13.97
O19	Axial	300(0)	15(-∝)	3(0)	14(0)	12.08
O20	Axial	300(0)	75(+∝)	3(0)	14(0)	17.01
O21	Axial	300(0)	45(0)	1(-∝)	14(0)	11.08
O22	Axial	300(0)	45(0)	5(+∝)	14(0)	14.51
O23	Axial	300(0)	45(0)	3(0)	2(-∝)	18.27
O24	Axial	300(0)	45(0)	3(0)	26(+∝)	14.24
O25	Centre	300(0)	45(0)	3(0)	14(0)	18.78
O26	Centre	300(0)	45(0)	3(0)	14(0)	18.40
O27	Centre	300(0)	45(0)	3(0)	14(0)	20.52
O28	Centre	300(0)	45(0)	3(0)	14(0)	20.73
O29	Centre	300(0)	45(0)	3(0)	14(0)	18.51
O30	Centre	300(0)	45(0)	3(0)	14(0)	19.69

Scanning Electron Microscopy (SEM, Fei Quanta 400 F, Hillsboro, OR, USA) was used to examine the porous structure distribution in the carbon cryogels. Energy-Dispersive X-ray Spectroscopy (EDX) was utilized to check the elemental analysis and distribution, with samples prepared similarly to those for SEM analysis and coated with a conductive layer. Specific regions were selected for EDX mapping using the X-Max detector at a 35° angle and an accelerating voltage of 20 kV.

The surface area, pore size, and volume of catalyst samples were evaluated using standard N_2 physisorption with a Micromeritics ASAP2020 analyzer. Samples were outgassed in a vacuum at 300 °C for 10 h before N_2 physisorption. Surface area was determined using the BET method, and micropore and mesopore distributions were estimated using the t-plot and Barrett, Joyner and Halenda (BJH) methods, respectively.

Total acidity was determined through two distinct methods. First, temperature-programmed desorption of ammonia (NH_3-TPD) was employed using the TPDRO 1100 series (Thermo Electron). The instrument was cleaned with a 20 mL min^{-1} nitrogen flow for 5 min. A 500 mg catalyst sample was then degassed at 150 °C for 30 min under a constant nitrogen flow (20 mL min^{-1}), cooled to 50 °C, and ammonia was adsorbed for 1 h. After achieving saturation, nitrogen purging was conducted for 30 min at 20 mL min^{-1} to eliminate excess ammonia. The catalyst was subsequently heated from 50 to 800 °C for 1 h under a helium flow (20 mL min^{-1}) at a ramping rate of 10 °C min^{-1}, and the concentration of desorbed ammonia was quantified using a thermal conductivity detector (TCD).

Total acidity, representing acid density, was also determined using the acid-base titration method [41]. A 100 mg catalyst sample was mixed with 100 mL of 0.1 M NaOH solution and stirred at 145 rpm at room temperature overnight. The solution was then back-titrated with 0.5 M HCl until a neutral pH was achieved. These measurements were conducted in triplicate for accuracy.

The Hammett acidity function (H_0) was utilized to assess the Brønsted-Lowry acidities of carbon cryogels incorporated with $H_3PW_{12}O_{40}$-Nb_2O_5, using 4-nitroaniline as the basic indicator due to its $pK(I)_{aq}$ value of 0.99. A 100 mg sample of the catalyst and a portion of the Hammett indicator ($3.07 \times$ 10–1 mmol L^{-1}) were dissolved in 20 mL of distilled water. The mixture was stirred for 12 h at room temperature, then filtered, and the absorbance was measured using a Cary 500 UV/Vis/NIR spectrophotometer at 360 nm [42], [43]. The Hammett value was determined using the calculation described in Eq. (7), where $pK(I)_{aq}$ represents the pK_a value of the aqueous indicator solution, and $[IH^+]_s$ and $[I]_s$ denote the molar concentrations of the protonated and unprotonated forms of the indicator:

$$H_o = pK(I)_{aq} + \log\left(\frac{[I]_s}{[IH^+]_s}\right) \quad (7)$$

Lewis acid sites were quantified by calculating the difference between the total acidity acquired through the titration method and the Brønsted-Lowry acid sites determined using the Hammett acidity function. This allowed for the deduction of the ratio of Brønsted-Lowry to Lewis acid sites.

The synergy factor of the carbon cryogel catalyst was calculated to assess its overall catalytic performance using Eqs. (8), (9), and (10) below. This factor helps determine if the combination of different catalytic components or sites results in a synergistic effect, making the supported acid- carbon cryogel more effective than its individual components.

$$\text{Synergy factor} = A/B \quad (8)$$

A represents selectivity of LA in the mixed acid system

B represents the theoretical selectivity of LA in the mixed-acid system (ratio of Brønsted-Lowry acid × selectivity of LA catalyzed by pure Brønsted-Lowry acid) + (ratio of Lewis acid × selectivity of LA catalyzed by pure Lewis acid)

$$\text{Selectivity}(\%) = \frac{\text{yield of LA}}{\text{LA conversion}} \times 100\% \quad (9)$$

$$\text{Conversion}(\%) = \frac{\text{mass of cellulose reacted}}{\text{initial mass of cellulose}} \times 100\% \quad (10)$$

3. Results and discussion

3.1. Optimization and parametric influence via RSM

Table 3 highlights the performance variations of the carbon cryogel based on key factors observed during the synthesis process, including the ratio of $H_3PW_{12}O_{40}$ to Nb_2O_5, calcination time and temperature, and solvent exchange. Notably, during runs 25–30, the center points were replicated, showing small standard deviations in LA yield (ranging from 0.10 to 0.52). This indicated high repeatability and reproducibility, confirming the reliability of the optimized conditions.

Numerical optimization using RSM revealed that the maximum LA yield (20.1 %) was achieved by setting the calcination temperature and time, the ratio of $H_3PW_{12}O_{40}$ to Nb_2O_5, and solvent exchange time at 336 °C, 51.4 min, 3.02, and 9.2 h, respectively. The model was validated with triplicate data (Table 4), resulting in an error of less than 5 %. The experimental LA yield was 20.2 %, with a standard deviation of 0.36. The proposed model for LA yield in terms of coded factors is represented in Eq. (11):

$$\text{Yield} = 19.44 + 1.23\,A + 0.45B + 0.72\,C - 0.88D - 0.08AB - 0.01AC - 0.23AD + 0.02BC - 0.81BD + 0.85CD - 1.93A^2 - 1.25B^2 - 1.68C^2 - 0.82\,D^2 \quad (11)$$

3.1.1. RSM contour plots

Fig. 2 shows that all 3D surface plots exhibit a curved shape while keeping two variables constant. This curvature indicates interactions or higher-order effects between the factors, suggesting that a linear model may not adequately capture the relationship. This implies that the impact of the factors on the response is not constant and changes with variations in factor levels. There might be a combined effect of both factors that differ from the sum of their individual effects, a hypothesis to be further validated through statistical analysis in Section 3.1.2.

Each 3D surface plot in Fig. 2 presents a distinct response pattern derived from the RSM model. In Fig. 2a, the contour indicates a consistent influence of calcination temperature (200–400 °C) and time (30–60 min) on LA yield, signifying that increasing both parameters leads to a higher yield. In Fig. 2b, the simultaneous increase in calcination temperature and the ratio of Brønsted-Lowry to Lewis acid promotes the yield of LA, reaching an optimum point (20.1 %) where the value starts to decrease. Fig. 2c demonstrates an increasing LA yield with rising calcination temperature, in contrast to decreasing solvent exchange. Fig. 2d indicates that the increasing pattern of calcination time aligns with an increasing ratio of Brønsted-Lowry to Lewis acid, meaning both factors affect LA yield in the same direction. Meanwhile, the interactions between factors B and D and between factors C and D in Figs. 2e and 2f, respectively, show an opposite direction as LA yield increases or decreases.

3.1.2. RSM statistical analysis

The proposed model demonstrates robust predictive performance, as evidenced by an R^2 value of 0.95, indicating that 95 % of the variation in LA yield can be explained by the selected process variables. The coefficient of variation (6.46 %) reflects consistent response reliability across the experimental design. Strong agreement between observed and predicted values is further confirmed by the adjusted R^2 (0.90) and predicted R^2 (0.80). ANOVA results (Table 5) reveal that both linear and

Table 4
Optimization of carbon cryogel attributes and validation for LA yields.

Experiment	Calcination temperature (°C)	Calcination time (min)	Ratio of $H_3PW_{12}O_{40}$ to Nb_2O_5	Solvent exchange time (h)	Response (%)	Error (%)
					LA yield	
CCD	336	51.4	3.02	9.2	20.10	
Validation (Trial 1)	336	51.4	3.02	9.2	19.99	
Validation (Trial 2)	336	51.4	3.02	9.2	20.00	
Validation (Trial 3)	336	51.4	3.02	9.2	20.62	
Validation[a]	336	51.4	3.02	9.2	20.20	0.50

[a] Mean for triplicate data.

quadratic terms significantly influence LA yield. Among these, quadratic terms for calcination temperature (A^2, F-value=109.94) and $H_3PW_{12}O_{40}/Nb_2O_5$ ratio (C^2, F-value=83.81) are particularly dominant. The model's F-value of 21.02 ($p < 0.0001$) confirms its overall statistical significance, while the lack of fit F-value (0.82) indicates a good fit with the experimental data. An adequate precision value of 14.92, well above the desired threshold of 4, confirms that the model provides a reliable signal-to-noise ratio within the CCD design space.

Additional diagnostic plots (see Supplementary material) support the adequacy of the quadratic model. The normal probability plot of residuals shows overall alignment with the theoretical line, with minor deviations at runs 19 and 20 — consistent with expected behavior at axial (±α) design points that are purposefully placed beyond the central region to stretch the model's predictive capacity. The residuals vs. predicted values plot displays no significant curvature or funnel shape, indicating acceptable linearity and homoscedasticity. Externally studentized residuals are evenly scattered around the zero line, with no values exceeding the threshold (±3.87982), confirming the absence of outliers and validating model assumptions. The Box-Cox plot confirms that the LA yield data require no transformation, reinforcing the model's validity within the RSM framework. Low leverage values (0.2 and 0.5) and Cook's Distance values (mostly < 0.4) affirm that no single data point disproportionately influences the model.

Importantly, the model reflects how preparation parameters—including calcination temperature and time, solvent exchange duration, and $H_3PW_{12}O_{40}$-Nb_2O_5 ratio — affect the physicochemical properties of the cryogel catalyst. These properties (surface area, acidity, pore structure) are directly linked to LA yield. While some interaction terms (e.g., BD or CD) exhibit significant synergistic effects, others, especially those involving calcination conditions (AB, AC, AD), appear statistically insignificant. This may stem from the relatively narrow range of calcination conditions tested, or from indirect structural effects that are not immediately reflected in LA yield metrics. For instance, over-calcination could reduce active site density or cause pore collapse — impacts that may be masked if solvent exchange time plays a dominant kinetic role. Thus, even interaction terms with limited statistical weight may influence underlying physicochemical transformations, subtly shaping catalytic performance. Their practical relevance should not be discounted despite statistical insignificance.

3.2. Structural integration of acid components

Comprehensive physicochemical analyses revealed how synthesis parameters influence both activity and durability of the $H_3PW_{12}O_{40}$–Nb_2O_5–lignin–xanthan cryogel catalyst. XRD patterns (Supplementary material) confirmed the successful incorporation of Nb_2O_5's orthorhombic TT phase and the intact Keggin structure of $H_3PW_{12}O_{40}$, as evidenced by distinct low-angles peaks (7–11° 2θ). This preserved crystallinity underpins stable Brønsted and Lewis acidic frameworks essential for catalyst reusability and consistent LA yields. In a prior study [44], recycling tests showed the cryogel retained 97.5–81.8 % of its initial efficiency over five runs and still delivered 52.8 % efficiency after eight cycles, underscoring its structural resilience under repeated use.

With framework stability established, FTIR spectroscopy (Fig. 3) tracked functional-group transformations under varying calcination temperatures, acid ratios, and solvent exchange durations. Higher calcination temperatures removed organic templates and impurities, creating new active sites. For example, sample O8 (400 °C) exhibited shifts in C–H bands at 624 and 834 cm^{-1} , reflecting new bonding interactions among $H_3PW_{12}O_{40}$, Nb_2O_5, and lignin polymers. Characteristic Nb–O stretches at 640 and 990 cm^{-1} and Keggin P–O, W═O_t, and W–O–W vibrations at 1082, 972, and 890 cm^{-1} confirmed the integrity of each acid component [45], [46]. A synergistic band at 1132 cm^{-1} —resulting from overlapping P–O and Nb–O modes—intensified with higher $H_3PW_{12}O_{40}/Nb_2O_5$ ratios, signaling chemical integration [47], [48].

Sample OPT2 preserved strong aromatic C–H (1450–1500 cm^{-1}) and conjugated C═C (1500–1600 cm^{-1}) bonds at its optimal calcination temperature (336 °C), maintaining carbon backbone integrity and maximizing LA yield [49]. By contrast, samples calcined at 200 °C showed intensified C═C peaks—likely due to incomplete combustion of organic precursors. These conjugated linkages reinforce the cryogel's rigidity and thermal stability, indicating that native lignin and xanthan gum double bonds survive synthesis and contribute to durability.

Broad carbonyl peaks at 1700–1750 cm^{-1} —attributed to lignin–xanthan crosslinking—further modulate surface reactivity [50], while S–O stretching at 1150 [40] and 1050 cm^{-1} highlights sulfate anions chemisorbed on Nb_2O_5, forming M–O–SO_4 linkages that create superacidic Lewis/Brønsted pairs [38], [51], [52]. Calcination duration critically affects functional-group stability: extended heating can decompose labile moieties and degrade active sites. For example, sample O11—calcined at 200 °C for 60 min—exhibited weakened C–H (1450–1500 cm^{-1}) and C–O–C (1000–1200 cm^{-1}) bands, correlating with its reduced LA yield.

FTIR analysis also revealed O–H stretching bands at 2500–3100 cm^{-1}, 3200 cm^{-1}, and 3400–3650 cm^{-1}, corresponding to acidic, phenolic, and alcoholic groups (Supplementary material). The intensity of these bands varied with the Brønsted-Lewis acid ratio—evident in samples O8, O15, O22, and OPT2—reflecting shifts in surface acidity. Striking the right balance prevents pore collapse and active-site leaching while preserving functional-group accessibility. Solvent-exchange duration further modulated O–H vibrations: a 20 h exchange removed more organic residues and solvents, promoting larger pore formation, whereas shorter exchanges retained more material, yielding smaller pores. While in xanthan gum, absorption peaks at 3431 and 2922 cm^{-1} correspond to –OH stretching and sp^3 C–H vibrations [53], [54]; their disappearance after calcination confirmed O–H volatilization and pore development in the carbon cryogel template [40]. The resulting increase in surface hydrophobicity helps mitigate glucose overconversion and steers the reaction selectively toward LA instead of unwanted byproducts [55].

3.3. Morphological evolution and pore structure tuning

To engineer a pore network conducive to biomass conversion, the particle sizes of feedstock and synthesis reagents were deliberately explored (Table 6). SEM analysis confirmed a broad pore size distribution consistent with the nanoscale-to-microscale dimensions of the

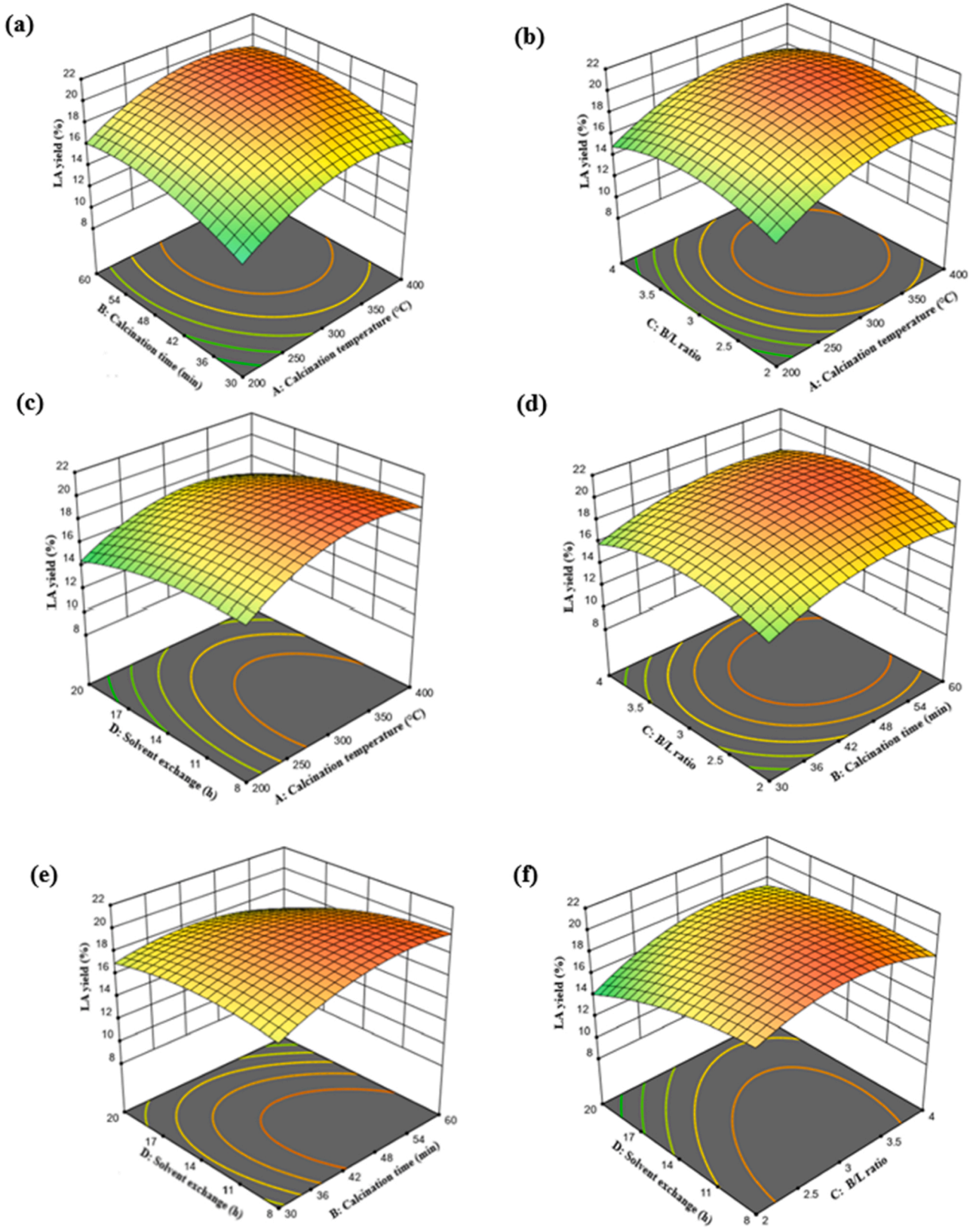

Fig. 2. RSM plots illustrating interaction effects between key synthesis parameters on LA yield: (a) calcination temperature and calcination time; (b) calcination temperature and B/L ratio ($H_3PW_{12}O_{40}$ to Nb_2O_5); (c) calcination temperature and solvent exchange duration; (d) calcination time and B/L ratio; (e) calcination time and solvent exchange duration; and (f) B/L ratio and solvent exchange duration. B/L: molar ratio of Brønsted acid ($H_3PW_{12}O_{40}$) to Lewis acid (Nb_2O_5).

Table 5
Statistical analysis for each response variable and the interaction terms.

Source	Sum of squares	Df	Mean of square	F-value	*p*-value	Std error	Remark
Model	272.580	14	19.470	21.020	< 0.0001		Significant
A – Calcination temperature (°C)	36.100	1	36.100	38.970	< 0.0001	0.20	
B – Calcination time (min)	4.760	1	4.760	5.140	0.0386	0.20	
C – Ratio of $H_3PW_{12}O_{40}$ to Nb_2O_5	12.580	1	12.580	13.580	0.0022	0.20	
D – Solvent exchange (h)	18.660	1	18.660	20.140	0.0004	0.20	
A^2	101.850	1	101.850	109.9400	< 0.0001	0.18	
B^2	42.530	1	42.530	45.9100	< 0.0001	0.18	
C^2	77.640	1	77.640	83.8100	< 0.0001	0.18	
D^2	18.330	1	18.330	19.7900	0.0004	0.18	
AB	0.105	1	0.105	0.1130	0.7412	0.24	
AC	0.004	1	0.004	0.0040	0.9521	0.24	
AD	0.860	1	0.860	0.9280	0.3506	0.24	
BC	0.005	1	0.005	0.0050	0.9452	0.24	
BD	10.570	1	10.570	11.4100	0.0041	0.24	
CD	11.490	1	11.490	12.4100	0.0031	0.24	
Residual	13.900	15	0.926				
Lack of Fit	8.640	10	0.864	0.8219	0.6310		Not significant
Pure Error	5.260	5	1.050				
Cor Total	286.480	29					

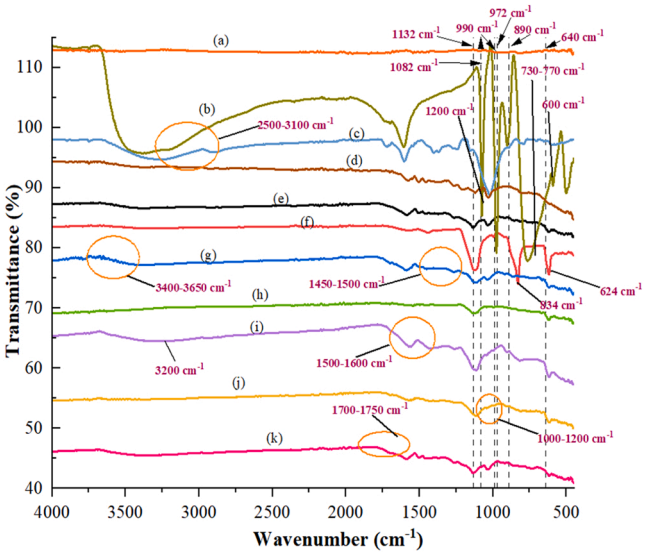

Fig. 3. FTIR spectra for carbon cryogel samples and raw precursor materials: (a) Nb_2O_5; (b) $H_3PW_{12}O_{40}$; (c) xanthan gum; (d) lignin; (e) O1; (f) O8; (g) O11; (h) O15; (i) O21; (j) O22; and (k) OPT2.

Table 6
Size of particles (materials used for cryogel synthesis) based on SEM visualization and ImageJ analysis.

Material	Range of size
DOPMF	400 nm – 40 μm
Lignin	4 – 30 μm
Xanthan gum	0.3 – 0.6 cm
$H_3PW_{12}O_{40}$	80 – 1000 μm
Nb_2O_5	60 – 180 μm
Carbon cryogel	10 nm – 180 μm

precursors. This range—especially evident in bulky components like lignin and DOPMF—suggests that both mesopore and macropore formation are governed by the inherent morphology of the starting materials.

FESEM imaging (Fig. 4) revealed that the resulting cryogels possess irregular and heterogeneously sized pores, indicating significant structural evolution during synthesis. These morphological features contribute to a diverse acid environment. Lignin's natural porosity and the sol-gel characteristics of xanthan gum create a robust framework. SEM micrographs revealed distinct features introduced by each acid catalyst: $H_3PW_{12}O_{40}$ generated rough, planar surfaces, while Nb_2O_5 imparted diamond-like structures. These observations highlight how synthesis variables shape the final cryogel morphology, which in turn governs catalytic behavior.

Among the carbon cryogel samples (Table 7), porosity varied notably with preparation conditions, primarily influenced by calcination temperature and acid strength. Sample OPT2 stood out with the highest pore volume and a well-developed hierarchical structure, enhancing interaction with biomass particles of various sizes. This hierarchical pore architecture is essential for catalytic performance—it increases acid site accessibility, facilitates mass transport, and supports sustained activity. EDX analysis of the optimized cryogel (Table 8) further confirmed structural integrity: carbon content remained stable post-calcination, while decreased oxygen levels pointed to volatilization of non-carbon species, consistent with pore formation.

Macropores play a critical role in allowing larger biomass fragments to access catalytic domains, particularly aiding cellulose hydrolysis. However, excessive macroporosity can reduce LA yields due to increased risk of side reactions such as fragmentation and polymerization [59], [60]. Hence, balancing pore sizes is crucial. A hierarchical structure enables sequential catalysis: macropores support biomass hydrolysis, while mesopores and micropores facilitate glucose dehydration and LA formation [60], [61]. Larger mesopores may also promote hydronium ion generation in aqueous media, boosting local Brønsted acidity and further enhancing reaction efficiency.

To quantify this structural balance, the Hierarchical Factor (HF) was used—defined as the product of relative mesoporosity (S_{meso}/S_{BET}) and microporosity (V_{micro}/V_{total}) [62]. HF serves as a useful indicator of transport efficiency within the pore network [63]. OPT2 exhibited a higher HF (0.035) compared to O15 (0.006), reflecting a favorable mesoporous-to-microporous ratio. Although lower than benchmark catalysts like Fe/HY zeolite (0.163) [56], this value suggests that pore tuning should be aligned with feedstock properties. In biomass conversion, a moderate HF appears more suitable, as bulky cellulose fragments must first access macropores before undergoing catalytic transformation.

Sample OPT2 achieves the highest LA yield due to a homogeneous distribution of acid sites, as shown in Fig. 5, and exhibits minimal impact from catalyst loss [44]. In contrast, other samples, such as O8, experience uneven acid site distribution, resulting in the leaching of phosphorus from $H_3PW_{12}O_{40}$ and niobium from Nb_2O_5. This leaching is attributed to calcination-induced oversaturation, where excessive active component loading at elevated temperatures leads to detachment from

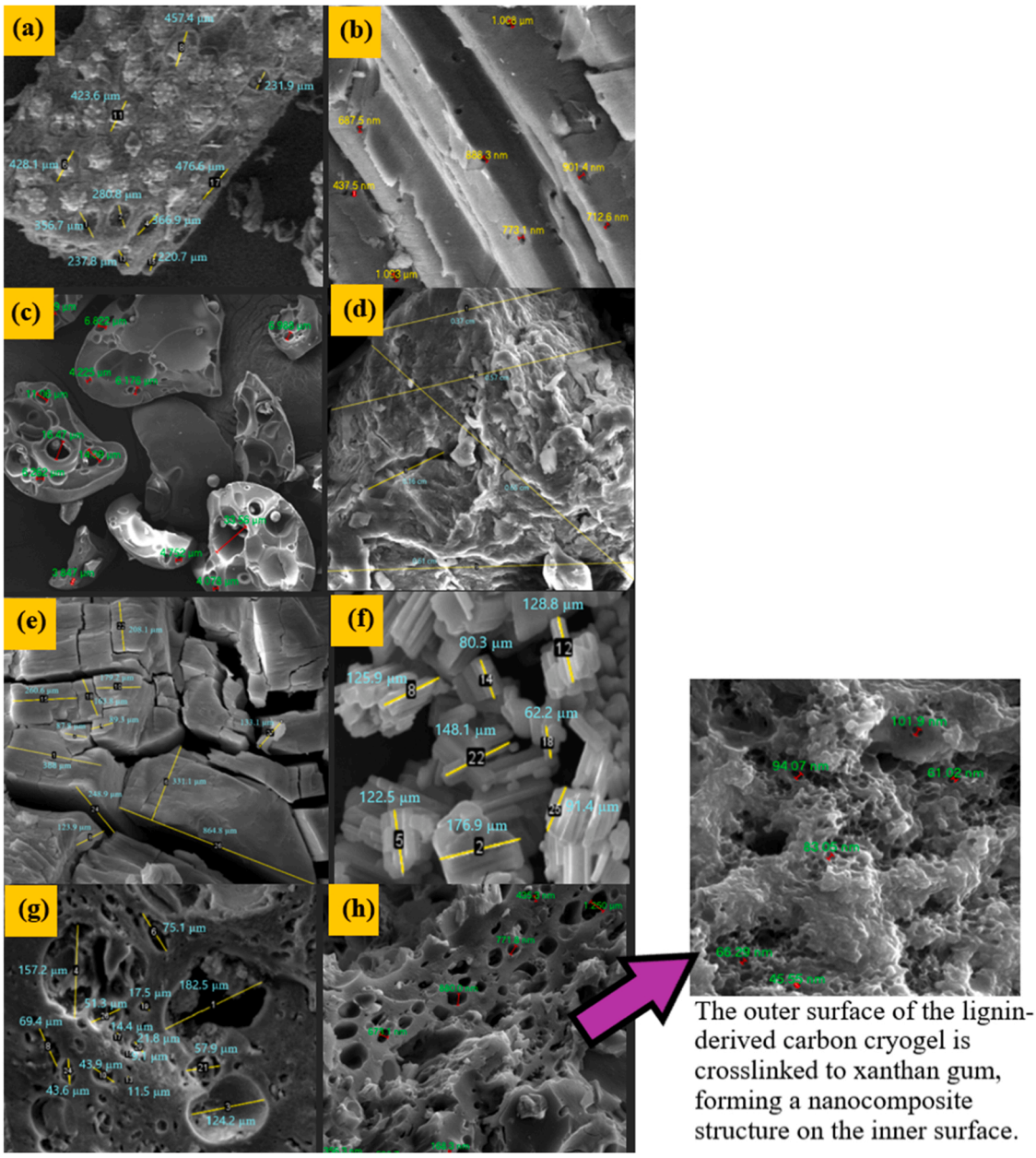

Fig. 4. FESEM images for sizes of raw materials: (a) DOPMF at micro scale; (b) DOMF at nano scale; (c) lignin; (d) xanthan gum; catalysts for (e) $H_3PW_{12}O_{40}$ and (f) Nb_2O_5; and synthesized carbon cryogel at (g) micro-scale and (h) nanoscale.

Table 7
Volume of pores of carbon cryogel samples compared to other catalysts.

Ref.	Catalyst sample	V_{pores} ($cm^3\ g^{-1}$)	V_{micro} ($cm^3\ g^{-1}$)	V_{meso} ($cm^3\ g^{-1}$)	V_{macro} ($cm^3\ g^{-1}$)	HF
This study	O1	0.008	–	–	0.008	–
This study	O8	0.009	–	–	0.009	–
This study	O11	0.032	–	0.0007	0.032	–
This study	O15	0.010	0.0001	0.0005	0.009	0.006
This study	O21	0.005	–	–	0.005	–
This study	O22	0.015	–	0.0030	0.012	–
This study	OPT2	0.156	0.0060	0.1000	0.050	0.035
[56]	HY zeolite	0.265	0.1670	0.0980	–	0.163
[57]	Fe-NbP	0.520	–	–	–	–
[58]	Carbon foam supported $H_5AlW_{12}O_{40}$	0.900	–	–	–	–

the cryogel framework. Notably, the agglomeration of niobium in localized regions generates concentrated acidic domains, which compromise structural integrity and increase susceptibility to degradation. Such degradation weakens acid site activity and, ultimately, reduces LA yield. The relevance of these findings is further supported by the morphological data presented in Fig. 6, where SEM

Table 8
EDX analysis for elements involved in carbon cryogel.

Sample	Element (%)							
	C	O	Na	K	P	W	Nb	S
Lignin	53.48	34.10	7.02	–	–	–	–	5.40
Xanthan gum	50.16	46.98	1.94	0.54	–	–	–	–
DOPMF	56.94	41.20	–	0.20	–	–	–	–
$H_3PW_{12}O_{40}$	7.55	27.46	–	–	1.11	63.42	–	–
Nb_2O_5	9.27	26.49	–	–	–	–	64.24	–
O1[a]	55.16	28.55	4.03	0.72	0.11	9.97	1.46	2.94
O8[b]	50.91	19.54	4.07	0.78	0.28	19.31	1.52	1.03
O11[a]	48.10	25.72	8.25	0.69	0.13	11.78	0.34	1.96
O15[b]	46.73	23.48	5.54	0.94	0.29	22.68	0.81	1.32
O21[c]	54.67	22.50	4.98	0.63	0.09	8.01	0.66	1.33
O22[d]	52.45	22.06	1.92	0.58	0.32	14.12	0.81	1.49
OPT2[e]	53.88	24.41	3.64	0.76	0.44	18.90	5.31	0.49

[a] 2:1
[b] 4:1
[c] 1:1
[d] 5:1
[e] 3.02:1

images reflect the pore features consistent with the EDX elemental distribution shown in Fig. 5. The visual correlation underscores how structural heterogeneity—particularly uneven acid side localization—can exacerbate catalyst vulnerability during thermal treatment.

Pore size also influences surface area and reactant accessibility. While micropores contribute significantly to surface area due to their high site density, their volume contribution is small compared to that of larger pores. The impact of pore size is also seen in O1 and O21, which showed large average pore diameters (111.93 nm and 176.31 nm, respectively). While macropores support initial hydrolysis, their dominance can suppress contributions from micropores—key for providing dense active site populations. These structural imbalances, along with potential by-product trapping in oversized pores, explain the limited catalytic performance and negligible HF values observed.

3.4. Surface properties and their impact on catalytic activity

Fig. 7 shows the low-pressure N_2 adsorption isotherms for the synthesized carbon cryogel samples. All samples exhibit convex-shaped curves with sharp uptakes as P/P_o approaches 1, corresponding to Type III isotherms according to IUPAC classification—characteristic of mesoporous materials with weak adsorbate–adsorbent interactions [64]. The accompanying Type H_3 hysteresis loops further indicate slit-shaped pores, commonly associated with structural heterogeneity and flexible frameworks [65].

The inclusion of xanthan gum in the cryogel formulations contributed to exceptionally low BET surface areas —below 0.8 $m^2 g^{-1}$ (Table 9**)** for samples O1, O8, O11, O21, and O22. This outcome stems for xanthan gum's dense, highly hydrophilic structure, poor gas adsorption behavior, and absence of intrinsic micro- or mesoporous features. As a result, accurate BET analysis was inherently limited for these samples. Nevertheless, low surface area alone did not correlate directly with catalytic performance, especially in LA production, reinforcing the importance of nuanced structure–activity relationships.

This paradox is explained by several interdependent factors:

1. Pore size and connectivity: BJH analysis revealed that macropores (>50 nm) dominated the pore architecture across all samples [66]. These large pores facilitated diffusion and transformation of bulkier biomass intermediates such as cellulose and glucose, indicating that pore connectivity and size are more critical to reactivity than surface area alone.
2. Acid site distribution and entrapment: Acid catalysts such as $H_3PW_{12}O_{40}$ and Nb_2O_5, introduced prior to lignin–xanthan gelation, became embedded within the polymer matrix. This configuration reduced measured surface area but ensured that Brønsted and Lewis acid sites remained well-dispersed and accessible through mesoporous channels. While this reduced the overall surface area, it ensured that Brønsted and Lewis acid sites were well-dispersed and accessible through mesoporous channels, maintaining high catalytic activity.
3. Structural modification by active components: Metal oxides and oxygen-rich species may have partially blocked micropores, decreasing surface area but increasing average pore diameter—an effect consistent with findings in Fe/HY zeolites and TPA/NbP systems [67].

Taken together, these factors affirm that catalytic performance depends not only on the quantity of acid sites but on their strategic integration within a hierarchical porous network. For example, sample OPT2, despite a lower acid site density (0.220 μmol m^{-2}), achieved the highest LA yield, outperforming sample O15 (12.02 μmol m^{-2}). This suggests that optimized pore architecture and accessible acidity are more decisive than raw acid loading, as excessive acidity in O15 likely caused unselective reactions and increased by-product formation [58].

Moreover, samples O8 and O22, despite low surface areas, demonstrated improved LA yields compared to O15. It is likely that high acid loading prompted carbon framework contraction, shrinking BET surface area while expanding internal void networks. Notably, O8 delivered a 16.5 % LA yield, potentially due to its 4:1$H_3PW_{12}O_{40}$:Nb_2O_5 ratio, which enhanced Brønsted acidity. However, excessive $H_3PW_{12}O_{40}$ may have caused pore blockage via polyphosphate formation [69], emphasizing the need for controlled acid incorporation.

Conversely, sample O11—with the highest total pore volume among this group—recorded the lowest LA yield (9.43 %). BJH pore analysis (Fig. 8**a**) revealed a structure dominated by macropores with minimal meso- or microporosity, limiting effective diffusion and intermediate conversion. Fig. 8**b** further confirms that pore volume and surface area do not scale proportionally. Despite O11's higher volume, its surface area was lower than that of O15, which featured richer meso- and micropore content. These smaller pores provide better surface-to-volume ratios and greater active site accessibility.

Solvent exchange duration also influenced porosity and performance. Extended exposure to *t*-butanol caused gel shrinkage and partial pore collapse, reducing pore connectivity and reactant accessibility. Sample O11 exemplified this effect, exhibiting diminished surface area and poor LA yield. Similar limitations appeared in O1 and O21, where inadequate exchange time, mild calcination, or weak catalyst embedding restricted pore formation and catalytic efficacy. Ultimately,

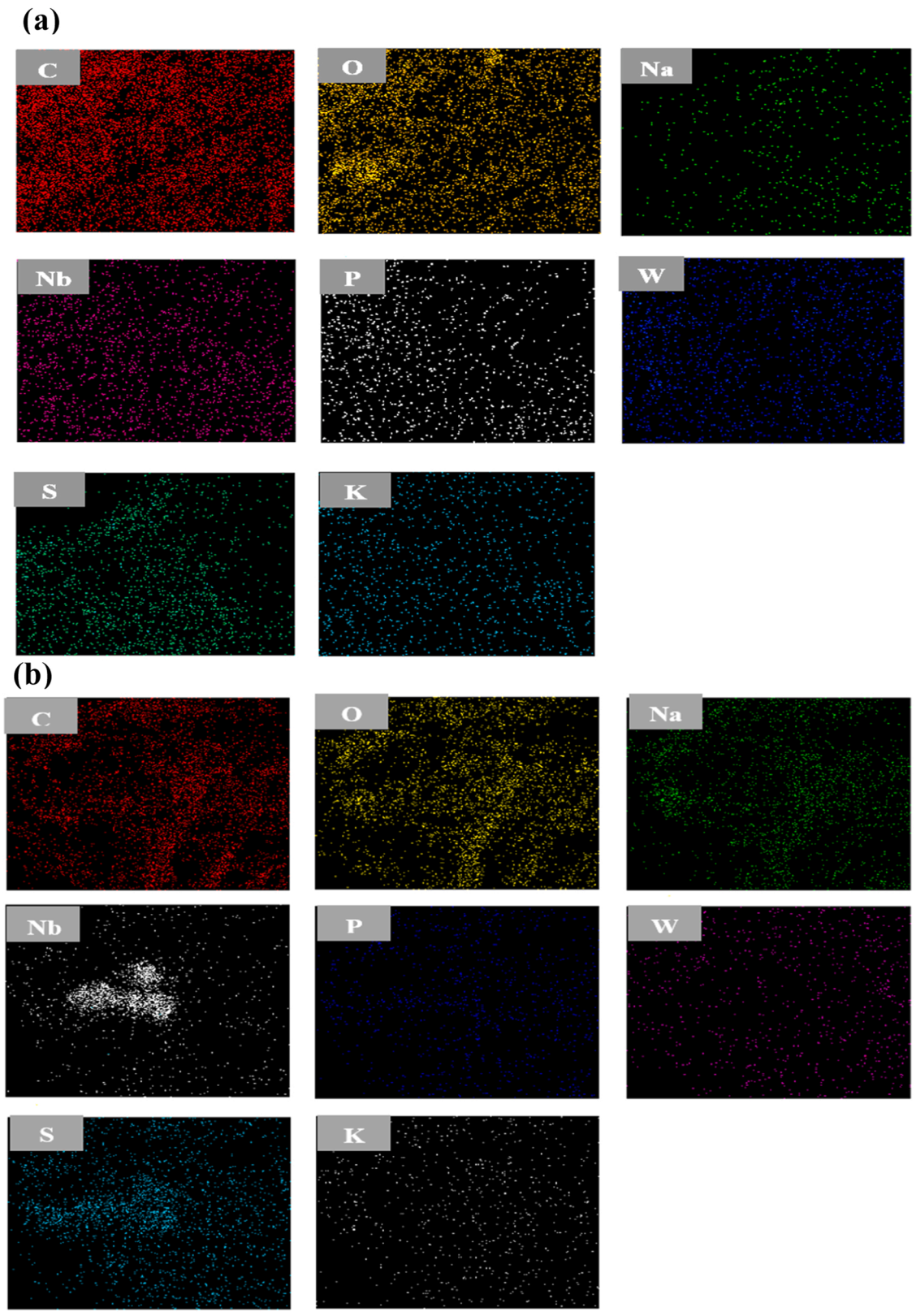

Fig. 5. EDX mapping for distribution of elements within the carbon cryogel for samples (a) OPT2 and (b) O8.

optimizing synthesis variables—including solvent exchange duration, calcination settings, and acid loading—is essential for achieving effective pore structure and acidity.

Importantly, the choice of raw material directly affects the catalyst's structure and reactivity. In this study, OPMF was selected as the feedstock due to its high cellulose and hemicellulose content, abundant availability in Malaysia, and low economic value as agro-industrial waste. Compared to other biomass sources, OPMF offers a favorable balance between carbohydrate richness and moderate lignin content, which enhances both reactivity and matrix stability during acid

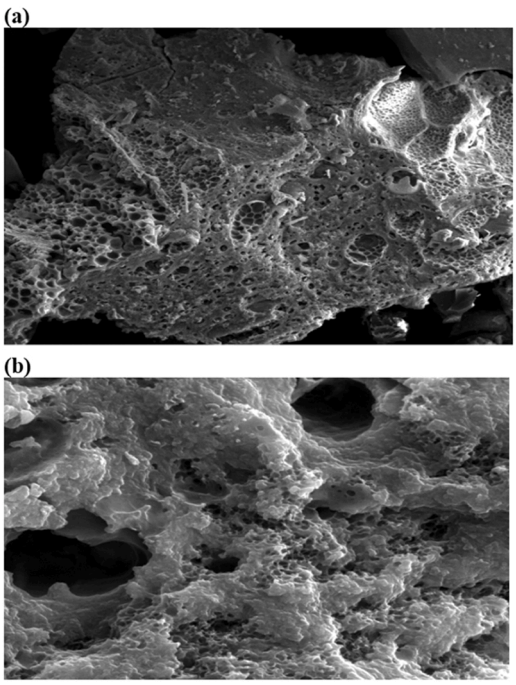

Fig. 6. SEM images of carbon cryogel samples: (a) OPT2 and (b) O8.

hydrolysis. Its chemical composition supports the formation of structurally robust cryogels and ensures efficient depolymerization pathways to glucose—an essential intermediate in LA production.

Therefore, while surface characteristics influence performance, the intrinsic composition of OPMF plays a vital role in facilitating optimal pore formation, acid-site dispersion, and catalytic output. The success of sample OPT2, which achieved a surface area of 57.41 m^2 g^{-1} and the highest LA yield, reinforces how raw material selection and tailored synthesis converge to create a mesoporous catalyst with efficient acidity and superior performance.

3.5. Acid site distribution and its influence on catalytic performance

The interplay between pore architecture and acid-site distribution emerges as a critical determinant of catalytic efficacy in LA production. While traditional metrics such as pore volume and surface area suggest accessibility advantages, our findings reveal that these characteristics alone do not guarantee higher yields. Instead, the catalytic performance is more significantly influenced by the strength, distribution, and synergy between Brønsted and Lewis acid sites embedded within the cryogel matrix. Sample OPT2, formulated via controlled solvent exchange and calcination, represents a benchmark in scaffold accessibility and acid-site balance. Despite its relatively low acid-site density, OPT2 yielded the highest LA conversion, attributable to an optimal concentration of medium-strength acid sites. This balance minimizes pore obstruction from acid–acid interactions and prevents structural degradation often observed in heavily loaded catalysts.

NH_3-TPD profiles (Fig. 9) demonstrate the presence of weak (100–350 °C), medium (350–600 °C), and strong (600–800 °C) acid sites across all samples. Crucially, total acidity and site distribution varied substantially. For example, samples O1, O11, and O15 recorded high acid-site densities, largely contributed by weak acid desorption (Table 10). These peaks are linked to loosely bound Brønsted OH groups that persist under mild calcination (~200 °C) [70], and their dominance correlates with underwhelming LA yields. Meanwhile, higher calcination temperatures (>300 °C) reduced the prevalence of weak sites by decomposing thermally unstable functionalities. In turn, this promoted the formation of medium and strong acid sites associated with residual phosphotungstic acid (Brønsted) and Nb^{5+} coordination complexes (Lewis) [71].

Sample O1, limited to 8 h of solvent exchange, retained excess labile species, contributing to elevated weak acidity [45]. Conversely, extended solvent exchange in sample O21 resulted in gel shrinkage and pore collapse. This restructuring concentrated medium-strength acid sites within tortuous channels, reducing accessibility and hampering LA synthesis. The condition also introduced mass-transfer limitations, as reactants struggled to diffuse into restricted pore networks. Sample O22, despite its high acid-site ratio (5:1), achieved a modest 14.5 % LA yield. The relatively short calcination time (45 min at 300 °C) likely hindered full precursor decomposition, suppressing strong acid-site formation. Conversely, prolonged calcination enhances acid-site anchoring by catalyzing dehydration and condensation reactions between $H_3PW_{12}O_{40}$, Nb_2O_5, and the carbon matrix.

Sample O8 displayed a distinct profile— rich in strong acid sites (4.577 mmol g^{-1}) and low in weak acidity—owing to its formulation (4:1$H_3PW_{12}O_{40}$—Nb_2O_5 ratio)—and elevated calcination temperature (400 °C). Nonetheless, its LA yield (16.5 %) was surpassed by OPT2 (20.2 %), which achieved a more balanced acidity spectrum and maintained moderate contributions across weak, medium, and strong sites. The tailored calcination conditions (336 °C, 51.4 min) preserved oxygenated groups, amplifying medium-strength acidity and catalytic performance.

The cryogel framework incorporating $H_3PW_{12}O_{40}$ and Nb_2O_5 offers a tunable acid environment via Brønsted—Lewis site coexistence. The optimized catalyst exhibited a total acidity of 12.66 mmol g^{-1} —surpassing traditional benchmarks such as HY zeolite (2.68 mmol g^{-1}) [56], pure $H_3PW_{12}O_{40}$ (2.46 mmol g^{-1}) [72], sulfonated carbon fiber (2.43 mmol g^{-1}) [73], and Fe-impregnated zeolites (2.81 mmol g^{-1}) [56]. This enhancement is not solely due to individual acid strengths but to their synergistic interactions: Nb_xO_y species contribute Lewis acidity for C–O bond cleavage, while $H_3PW_{12}O_{40}$ ensures robust proton donation through Brønsted functionality. Furthermore, spectroscopic analysis confirms structural preservation of the Keggin unit and promotes effective electronic coupling between Nb_2O_5 and the carbon framework—amplifying acid strength beyond additive contributions. Some formulations reached up to 20.38 mmol g^{-1} compared to other carbon-based catalysts (typically below 9.0 mmol g^{-1}), placing the system among the most potent carbon-based solid acids in biomass valorization [74].

Additionally, microwave-assisted hydrolysis, employed across all reactions, provided rapid thermal transfer, reducing side reactions and acid site deactivation. This approach helped retain strong acid sites under demanding conditions and enhanced overall catalyst stability. Microstructural variations among samples stemmed from deliberate and statistically controlled synthesis parameters, ensuring meaningful interpretation of synthesis—property—performance relationships.

3.6. Brønsted–Lewis acidity balance and synergistic catalysis in cryogel systems

To deepen the understanding of acid-site characteristics beyond total acidity (as revealed by NH_3-TPD), the Hammett acidity function (H_0) and acid–base titration were employed to differentiate Brønsted from Lewis acid contributions. While NH_3-TPD offers a comprehensive measure of acid content, it does not distinguish acid type. In contrast, the Hammett approach, coupled with UV-Vis spectroscopy (Fig. 10), selectively assesses Brønsted proton-donating strength across cryogel formulations.

As shown in Table 11, stronger Brønsted acidity correlates with lower H_0 values [43]. Sample O8 displayed the highest Brønsted strength (H_0 = 0.995), followed closely by O22 and OPT2. These values are comparable to those reported for other heteropoly acid-derived catalysts (H_0 = 0.41–0.63) [41], confirming the strong proton donation capacity of $H_3PW_{12}O_{40}$ within the cryogel matrix.

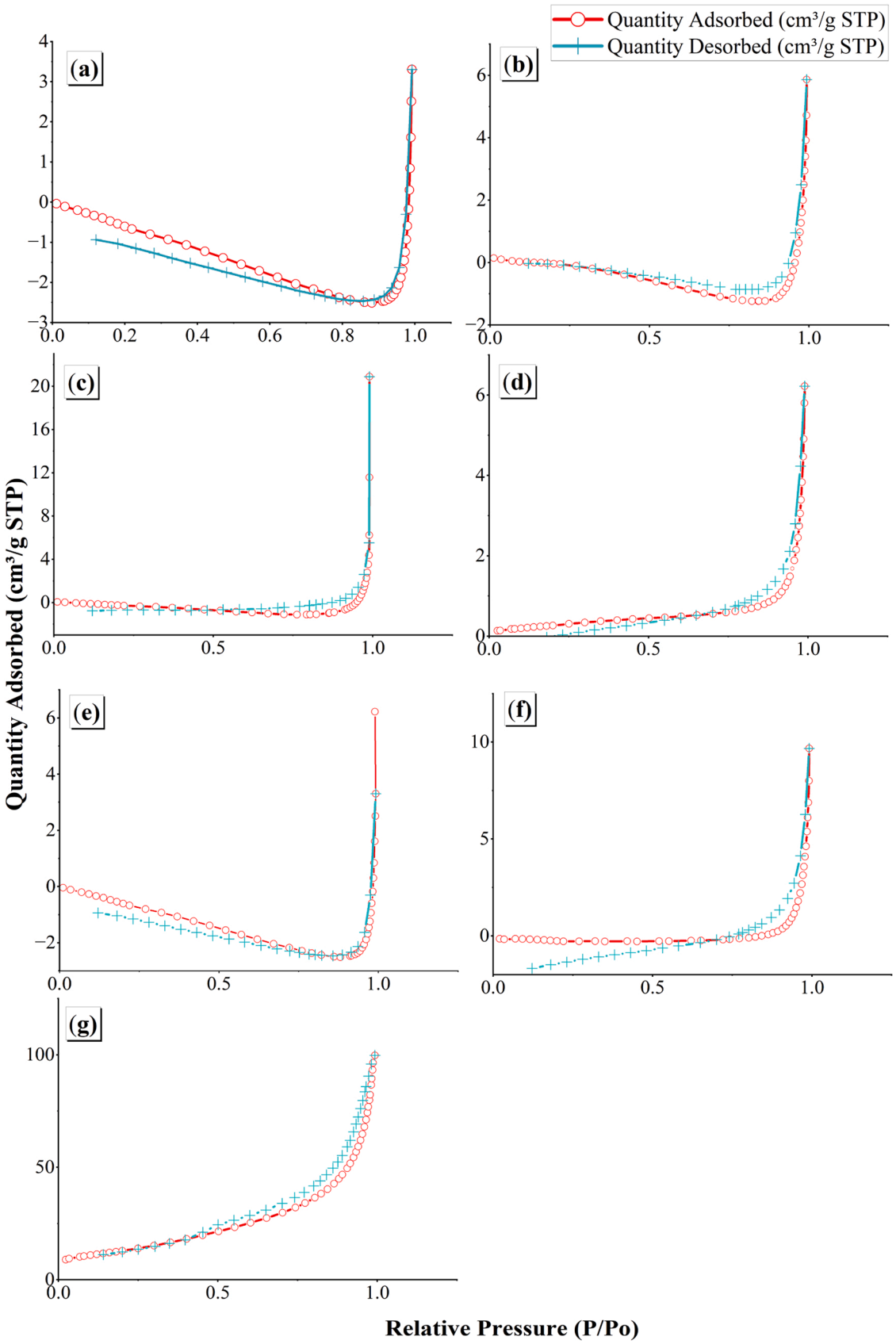

Fig. 7. N_2 adsorption-desorption isotherm for (a) O1; (b) O8; (c) O11; (d) O15; (e) O21; (f) O22; and (g) OPT2.

Table 9
Textural properties of studied carbon cryogels and other types of catalyst.

Ref.	Catalyst	Feedstock	Single point ($m^2 g^{-1}$)	Langmuir ($m^2 g^{-1}$)	t-plot ($m^2 g^{-1}$)	S_{BET} ($m^2 g^{-1}$)	S_{micro} ($m^2 g^{-1}$)	S_{meso} ($m^2 g^{-1}$)	S_{macro} ($m^2 g^{-1}$)	Acid sites (μmol m^{-2})	Pore size (nm)	LA yield (%)
Lignocellulosic biomass												
This study	$H_3PW_{12}O_{40}$	DOPMF	4.80	6.53	1.77	3.52	0.10	3.03	0.20	1.243	16.36	8.40
This study	Nb_2O_5	DOPMF	0.81	1.10	0.31	0.36	0.04	0.26	0.06	0.077	31.55	10.90
This study	O1	DOPMF	–	–	–	0.29	–	0.03	0.26	58.620	111.93	12.40
This study	O8	DOPMF	0.01	0.01	1.25	0.30	–	–	0.30	30.330	123.46	16.52
This study	O11	DOPMF	–	–	–	0.87	–	0.07	0.80	18.970	149.11	9.43
This study	O15	DOPMF	0.92	1.60	1.61	1.29	0.21	0.83	0.26	12.020	29.72	12.82
This study	O21	DOPMF	–	–	–	0.11	–	–	0.11	132.730	176.31	11.08
This study	O22	DOPMF	–	–	–	0.52	–	0.43	0.09	23.650	71.45	14.51
This study	OPT2	DOPMF	44.72	63.90	44.85	57.41	1.85	53.11	2.45	0.220	10.88	20.20
[68]	Multifunctional sulfonated humins	Bamboo	–	–	–	1.90	–	–	–	2.110	1.00	45.60
Monosaccharide												
[56]	10 % Fe/HY zeolite	Glucose	–	–	–	549.30	133.60	415.80	–	0.005	1.89	62.00
Polysaccharide												
[57]	Fe-NbP	Cellulose	–	–	–	305.41	–	–	–	0.012	6.82	64.20
[58]	Carbon foam supported $H_5AlW_{12}O_{40}$	Cellulose	–	–	–	5.60	–	–	–	0.131	668.40	61.90
[58]	Carbon foam	Cellulose	–	–	–	7.30	–	–	–	–	1220.00	8.90

S_{BET} for DOPMF is 0.12 $m^2 g^{-1}$ and its average pore size is 161.47 nm.

What sets this system apart, however, is the enhanced performance achieved through synergistic integration with Nb_2O_5. Structural interactions between Nb^{5+} and WO_3^- species lead to the formation of Nb–O–W frameworks via hydrogen bonding [75]. This results in a cooperative acid environment where niobium stabilizes Brønsted domains, reinforces acid-site density, and promotes active site formation—particularly at oxide interface regions [76]. The dual-phase contribution not only amplifies the reactivity of individual acids but also enables their co-functionality during complex catalytic steps.

Nb_xO_y species further enrich this synergy by introducing Lewis acid sites with unique electronic configurations. The Nb^{5+} centers are adept at facilitating C–O bond scission and dehydration processes essential to biomass transformation [77]. Together, Brønsted sites initiate hydrolysis (e.g. cleavage of β-1,4 glycosidic bonds), while Lewis sites support downstream isomerization and condensation reactions—making the tandem interplay key to enhancing product selectivity and LA yield.

Table 12 reinforces this conclusion: among various formulations, OPT2 exhibited the most balanced acidity profile, with a Brønsted/Lewis ratio of 1.48 and total acidity of 12.50 mmol g^{-1}. This balance contributed to the highest observed LA yield (20.2 %) and the strongest calculated synergy factor (SF = 2.15). In contrast, sample O11—with the lowest SF (0.94) and an imbalanced acid ratio—suffered from diminished yield despite having high total acidity, illustrating that cooperative balance is more vital than sheer acid concentration.

Catalyst calcination conditions further impacted the balance between acid types. A temperature of 336 °C was found optimal, providing sufficient thermal activation while preserving the integrity of the organic cryogel heteropolyoxotungstate and oxide functionalities. At this temperature, acid strength is enhanced without compromising the physical framework or causing excessive acid-site leaching.

While inorganic components such as $H_3PW_{12}O_{40}$ and Nb_2O_5 remain catalytically active up to 400 °C [37], the cryogel's organic backbone—primarily composed of polymers like xanthan gum—begins to degrade above 250 °C, leading to pore collapse and diminished accessibility. Therefore, moderate calcination serves as a crucial compromise, preventing structural deterioration while still enabling the formation of functional acid domains. This condition also supports the harmonious development of Brønsted and Lewis sites, aligning with previous findings that Brønsted acid formation increases up to ~1123 K, while Lewis acidity tends to diminish with thermal exposure [76]. Notably, samples such as O1, O11, and O15, calcined at a lower temperature of 200 °C, exhibited elevated Lewis acidity—likely due to incomplete transformation of Nb_2O_5, which in turn restricted Brønsted site accessibility.

Sample O8 exemplifies this synergy by achieving a high LA yield (16.5 %) despite fewer Lewis sites. Its success stemmed from elevated $H_3PW_{12}O_{40}$ loading and a shortened solvent exchange duration, fostering robust Brønsted domains and maintaining structural integrity. Meanwhile, sample OPT2 demonstrated how fine-tuning synthesis variables—acid ratio, calcination time, and solvent exchange—can orchestrate a co-dependent network of Brønsted–Lewis sites, yielding exceptional catalytic results.

While the cryogel synthesis method developed in this study is effective at the laboratory scale, scaling up presents inherent challenges in maintaining batch uniformity and structural consistency. In particular, achieving homogeneous crosslinking, uniform acid dispersion, and efficient solvent exchange across larger volumes may require process modifications such as continuous mixing, optimized mold geometry, or semi-automated freeze-drying protocols. Nonetheless, the use of biopolymer-based matrices and mild conditions offers promise for eco-friendly scale-up with potential adaptation to pilot-scale systems, provided the parameters identified through CCD optimization are carefully controlled.

Taken together, these findings highlight the nonlinear yet cooperative relationship between acid-site type and catalyst performance. Rather than favoring dominance by one acidity class, the cryogel system's strength lies in its ability to harmonize both—leveraging the

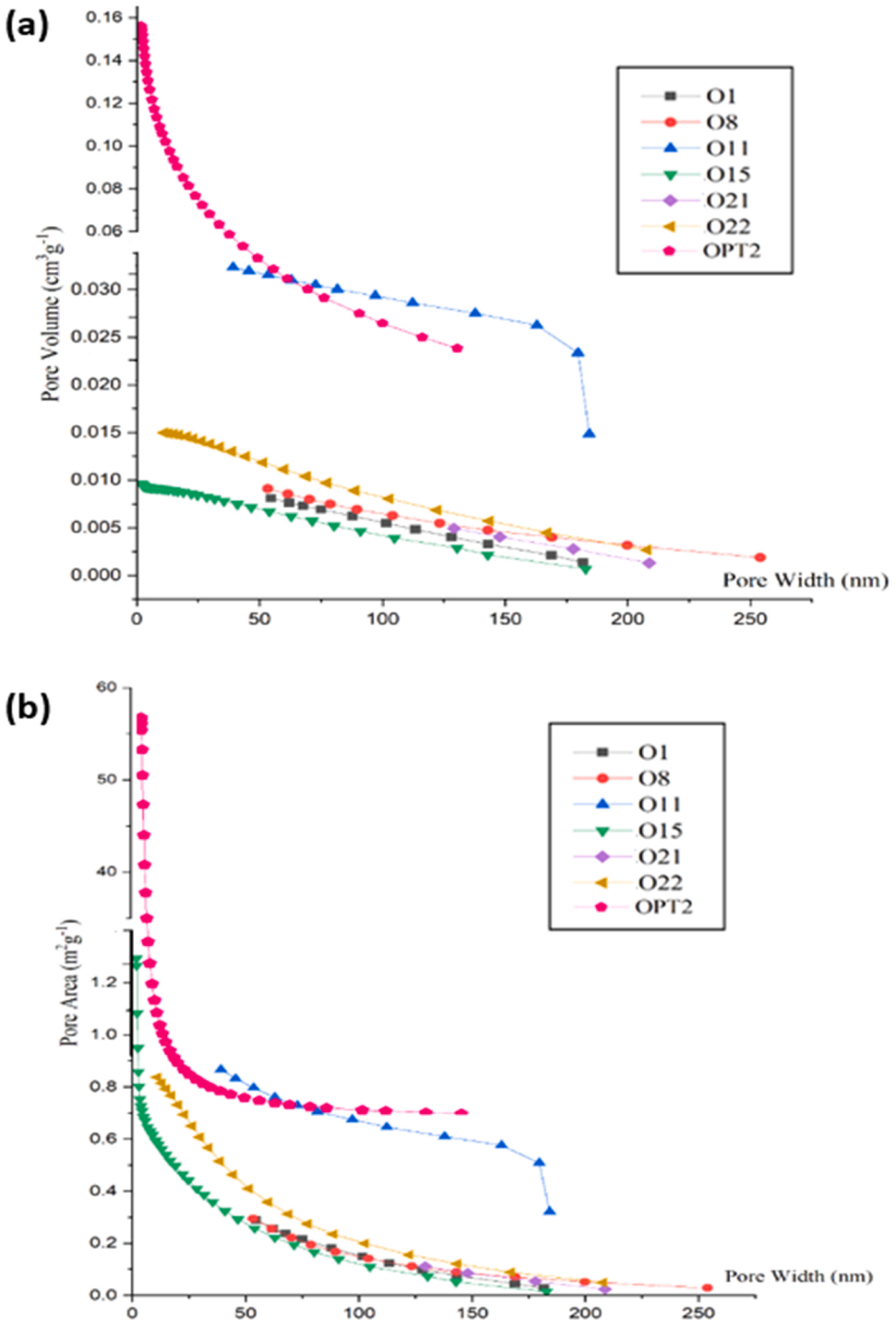

Fig. 8. BJH adsorption isotherm for assessing pore distribution across (a) pore volume; (b) pore area.

structural reinforcement of Nb_2O_5 with the proton mobility of $H_3PW_{12}O_{40}$. This synergy enables efficient one-pot biomass conversion, minimal side reactions, and scalable potential for LA synthesis.

4. Conclusion

This study underscores the critical importance of tailoring catalyst design to achieve optimal performance in biomass conversion. By employing a sol-gel synthesis approach, $H_3PW_{12}O_{40}$ and Nb_2O_5 were successfully anchored onto a lignin-based carbon cryogel support, creating a sustainable and structurally resilient catalyst. This formulation enabled efficient, one-pot LA synthesis under mild reaction conditions.

Optimization of key synthesis parameters—including the $H_3PW_{12}O_{40}$:Nb_2O_5 ratio, calcination temperature and duration, and solvent exchange time—revealed a complex interplay between acidity profiles and reaction performance. The optimized sample achieved the highest LA yield of 20.1 %, which corresponded with a well-balanced acidity dominated by medium-strength acid sites. Notably, excessive calcination temperatures diminished these medium sites and triggered undesired side reactions due to an overabundance of strong acidity.

Despite having a relatively modest surface area (57.41 $m^2\ g^{-1}$) and

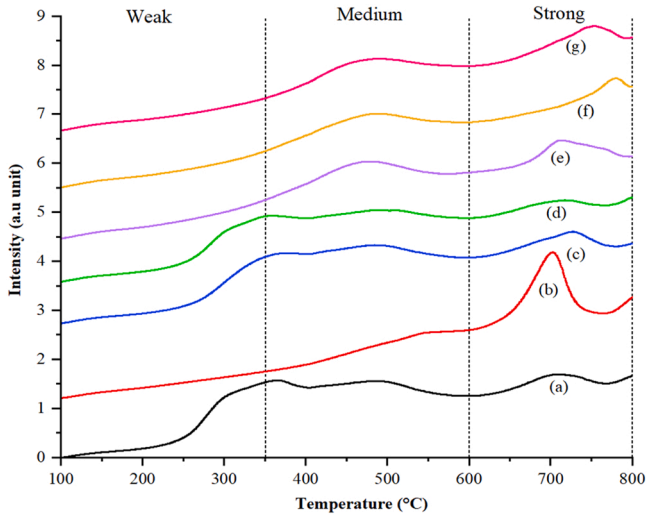

Fig. 9. Acid density by NH_3-TPD for samples (a) O1; (b) O8; (c) O11; (d) O15; (e) O21; (f) O22 and (g) OPT2.

Table 10
Strength of acid sites of different conditions of carbon cryogel synthesis.

Sample	Acid Density (mmol g^{-1})			
	Weak	Medium	Strong	Total
O1	9.356	5.815	1.967	17.138
O8	0.581	3.129	4.577	8.287
O11	7.632	5.708	2.522	15.862
O15	7.651	5.379	1.999	15.029
O21	1.186	9.200	2.634	13.020
O22	1.150	8.347	2.417	11.914
OPT2	1.556	7.867	3.234	12.657

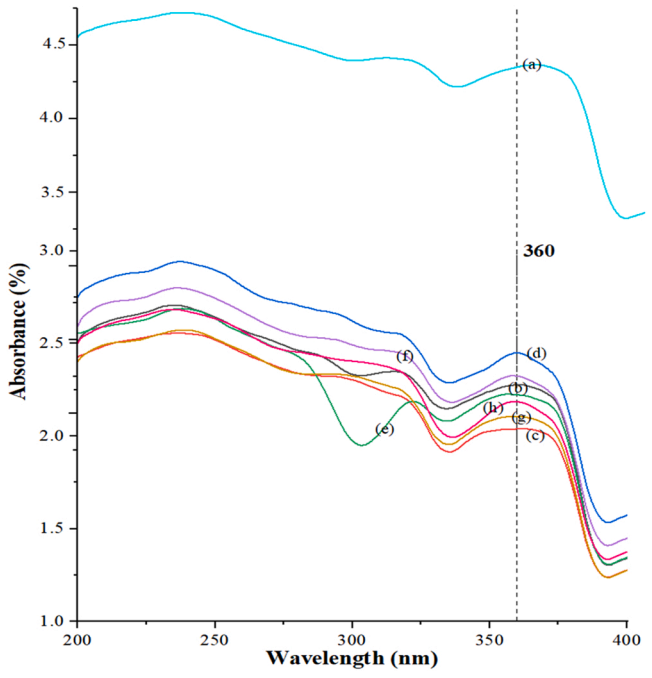

Fig. 10. UV-Vis spectra represents Hammett acidity function for selected carbon cryogel samples (a) blank, (b) O1, (c) O8, (d) O11, (e) O15, (f) O21, (g) O22 and (h) OPT2.

Table 11
Hammett acidity function for cryogel samples.

Sample	A_{max}	[I] %	[IH] %	H_o
Blank	4.388	100.00	0.00	-
O1	2.281	52.91	47.09	1.041
O8	2.167	50.26	49.74	0.995
O11	2.449	56.81	43.19	1.109
O15	2.277	52.81	47.19	1.039
O21	2.286	53.03	46.97	1.043
O22	2.193	50.87	49.13	1.005
OPT2	2.213	51.32	48.68	1.013

Table 12
Distribution of Brønsted-Lowry and Lewis acid sites in carbon cryogel prepared at different conditions of calcination, acid treatment and solvent exchange duration.

Sample	Brønsted-Lowry acid sites (mmol g^{-1})	Lewis acid sites (mmol g^{-1})	Total acidity (mmol g^{-1})	Ratio of Brønsted-Lowry to Lewis	Synergy factor
O1	6.99	10.01	17.00	0.70	1.26
O8	7.77	1.33	9.10	5.85	1.88
O11	5.97	10.53	16.50	0.57	0.94
O15	7.02	8.48	15.50	0.83	1.31
O21	6.96	7.64	14.60	0.91	1.14
O22	7.58	4.72	12.30	1.61	1.55
OPT2	7.45	5.05	12.50	1.48	2.15

porosity (0.13 cm^3 g^{-1}), the optimized cryogel exhibited a highly accessible mesoporous structure that enhanced mass transport. This feature proved especially important during cellulose hydrolysis and glucose decomposition stages, facilitating efficient diffusion and reactivity within the pore network.

Crucially, the catalyst retained a homogeneous acid-site distribution post-treatment, indicating minimal structural loss following calcination and solvent exchange. Thermal processing effectively eliminated organic residues and transformed surface functionalities into catalytically active domains, further boosting LA yield. Spectroscopic analysis revealed a distinctive vibrational band at 1132 cm^{-1} —formed from the merging of the P–O stretch in $H_3PW_{12}O_{40}$ with the Nb–O vibration in Nb_2O_5—highlighting a strong electronic interaction between the acid components.

This synergistic interaction, quantified by a synergy factor of 2.15 in the optimized sample, was central to the catalyst's superior performance. Together, these findings demonstrate that finely tuned integration of Brønsted and Lewis acid sites within a mesoporous lignin-derived cryogel framework can significantly improve selectivity, reactivity, and overall sustainability in biomass-to-LA conversion.

CRediT authorship contribution statement

Nadiah Syafiqah Mohd Azlan: Writing – original draft, Visualization, Validation, Methodology, Investigation, Formal analysis, Data curation, Conceptualization. **Chiew Lin Yap:** Writing – review & editing, Visualization, Validation, Supervision, Resources, Project administration, Methodology, Funding acquisition, Conceptualization. **Yong Wei Tiong:** Writing – review & editing, Software, Methodology. **Suyin Gan:** Writing – review & editing, Validation, Supervision, Conceptualization. **Mohd Basyaruddin Abdul Rahman:** Writing – review & editing, Validation, Supervision.

Declaration of Competing Interest

The authors declare that they have no known competing financial interests or personal relationships that could have appeared to influence

the work reported in this paper.

Acknowledgements

We sincerely appreciate the generous support from the technical staff at the University of Nottingham Malaysia. Our gratitude extends to the i-CRIM lab staff at Universiti Kebangsaan Malaysia (UKM) and the NanoCat lab staff at Universiti Malaya (UM) for their assistance with sample analysis and characterization.

This research was funded by the Ministry of Higher Education (MOHE), Malaysia, under Grant No. FRGS/1/2019/STG01/UNIM/02/4.

Appendix A. Supporting information

Supplementary data associated with this article can be found in the online version at doi:10.1016/j.jece.2025.118641.

Data Availability

Data will be made available on request.

References

[1] G.C. Hayes, C.R. Becer, Levulinic acid: A sustainable platform chemical for novel polymer architectures, Polym. Chem. 11 (2020) 4068–4077, https://doi.org/10.1039/D0PY00705F.
[2] O. Ali Qamar, F. Jamil, M. Hussain, A.H. Al-Muhtaseb, A. Inayat, A. Waris, P. Akhter, Y.-K. Park, Feasibility-to-applications of value-added products from biomass: Current trends, challenges, and prospects, Chem. Eng. J. 454 (2023) 140240, https://doi.org/10.1016/j.cej.2022.140240.
[3] J.J. Bozell, L. Moens, D.C. Elliott, Y. Wang, G.G. Neuenscwander, S.W. Fitzpatrick, R.J. Bilski, J.L. Jarnefeld, Production of levulinic acid and use as a platform chemical for derived products, Resour. Conserv. Recycl. 28 (2000) 227–239, https://doi.org/10.1016 /S0921-3449(99)00047-6.
[4] M.A. Khan, B. Dharmalingam, S. Chuetor, Y.-S. Cheng, M. Sriariyanun, Comprehensive review on effective conversion of lignocellulosic biomass to levulinic acid, Biomass. Convers. Biorefin. (2023), https://doi.org/10.1007/s13399-023-04663-2.
[5] C. Liu, X. Lu, Z. Yu, J. Xiong, H. Bai, R. Zhang, Production of levulinic acid from cellulose and cellulosic biomass in different catalytic systems, Catalysts 10 (2020) 1006, https://doi.org/10.3390/catal10091006.
[6] L.D. Mthembu, R. Gupta, N. Deenadayalu, Advances in biomass-based levulinic acid production, Waste Biomass. Valoriz. 14 (2023) 1–22, https://doi.org/10.1007/s12649-022-01948-x.
[7] B. Girisuta, H.J. Heeres, Levulinic acid from biomass: synthesis and applications, in: Z. Fang, R.L. Smith Jr., X. Qi (Eds.), Production of Platform Chemicals from Sustainable Resources, Springer, Singapore, 2017, pp. 143–169.
[8] M. Signoretto, S. Taghavi, E. Ghedini, F. Menegazzo, Catalytic production of levulinic acid (LA) from actual biomass, Molecules 24 (2019) 2760, https://doi.org/10.3390/molecules24152760.
[9] A.A. Anugrah, R. Febrino, M.E. Toif, R. Ringgani, A. Budiman, Kinetic studies of levulinic acid production from acid-catalyzed hydrolysis of sugar cane bagasse, AIP Conf. Proc. 2751 (2023) 070001, https://doi.org/10.1063/5.0151957.
[10] E.S. Lopes, J.C.J. Gariboti, L.H.Z. Feistel, E.C. Rivera, R.M.I. Filho, L.P. Tovar, Acid hydrolysis-based sugarcane bagasse biorefining for levulinic acid production: Dynamic mechanistic modeling under varying operating conditions, Chem. Eng. Trans. 80 (2020) 217–222, https://doi.org/10.3303/CET2080037.
[11] M.S.A. Pradipta, N.R. Purnamasari, Y.S. Pradana, Levulinic acid synthesis from Indonesian sugarcane bagasse using two-step acid catalyzed treatment, AIP Conf. Proc. 2085 (2019) 020065, https://doi.org/10.1063/1.5095043.
[12] M.G. dos Santos, H.M. Fogarin, D.D. Virginio da Silva, K.J. Dussán, Bioprocess development for levulinic acid production using sugarcane biomass, Sustain. Chem. Pharm. 33 (2023) 101085, https://doi.org/10.1016/j.scp.2023.101085.
[13] N. Abdullah, F. Sulaiman, The oil palm wastes in Malaysia, in: M.D. Matovic (Ed.), Biomass Now: Sustainable Growth and Use, InTech, Rijeka, Croatia, 2013, pp. 75–99.
[14] N. Nunraksa, S. Rattanasansri, J. Praiboon, A. Chirapart, Proximate composition and the production of fermentable sugars, levulinic acid, and HMF from *Gracilaria fisheri* and *Gracilaria tenuistipitata* cultivated in earthen ponds, J. Appl. Phycol. 31 (2019) 683–690, https://doi.org/10.1007/s10811-018-1552-9.
[15] L. Santos, G. Fraga, D. Pontes, L. Campos, L. Pontes, L. Teixeira, Alternatives for the production of levulinic acid obtained from biomass, Quim. Nova 44 (2021) 1–11, https://doi.org/10.21577/0100-4042.20170773.
[16] S. Dutta, I.K.M. Yu, J. Fan, J.H. Clark, D.C.W. Tsang, Critical factors for levulinic acid production from starch-rich food waste: Solvent effects, reaction pressure, and phase separation, Green. Chem. 24 (2022) 163–175, https://doi.org/10.1039/D1GC01948A.
[17] J. Ahlkvist, J. Wärnå, T. Salmi, J.-P. Mikkola, Heterogeneously catalyzed conversion of nordic pulp to levulinic and formic acids, React. Kinet. Mech. Catal. 119 (2016) 415–427, https://doi.org/10.1007/s11144-016-1069-7.
[18] P.L. Dhepe, A. Fukuoka, Cellulose conversion under heterogeneous catalysis, ChemSusChem 1 (2008) 969–975, https://doi.org/10.1002/cssc.200800129.
[19] S.-H. Pyo, S.J. Glaser, N. Rehnberg, R. Hatti-Kaul, Clean production of levulinic acid from fructose and glucose in salt water by heterogeneous catalytic dehydration, ACS Omega 5 (2020) 14275–14282, https://doi.org/10.1021/acsomega.9b04406.
[20] P. Sudarsanam, R. Zhong, S. Van den Bosch, S.M. Coman, V.I. Parvulescu, B.F. Sels, Functionalised heterogeneous catalysts for sustainable biomass valorisation, Chem. Soc. Rev. 47 (2018) 8349–8402, https://doi.org/10.1039/C8CS00410B.
[21] Z. Ma, X. Xing, Z. Qu, Y. Sun, G. Sun, X. Wang, Y. Han, Activity of microporous lignin-derived carbon-based solid catalysts used in biodiesel production, Int. J. Biol. Macromol. 164 (2020) 1840–1846, https://doi.org/10.1016/j.ijbiomac.2020.08.002.
[22] Y. Wang, F. Delbecq, W. Kwapinski, C. Len, Application of sulfonated carbon-based catalyst for the furfural production from d-xylose and xylan in a microwave-assisted biphasic reaction, Mol. Catal. 438 (2017) 167–172, https://doi.org/10.1016/j.mcat.2017.05.031.
[23] S. Xiong, Y. Guan, C. Luo, L. Zhu, S. Wang, Critical review on the preparation of platform compounds from biomass or saccharides via hydrothermal conversion over carbon-based solid acid catalysts, Energy Fuels 35 (2021) 14462–14483, https://doi.org/10.1021/acs.energyfuels.1c02672.
[24] J. Guo, Y. Yao, X. Yan, X. Meng, Q. Wang, Y. Zhang, S. Yan, X. Zhao, S. Luo, Emerging carbon-based catalysts for the oxygen reduction reaction: insights into mechanisms and applications, Inorg. (Basel) 12 (2024) 303, https://doi.org/10.3390/inorganics12120303.
[25] N. Wang, L. Wang, H. Xie, Y. Liu, Y. Sun, C. Yang, C. Ge, Preparation of high temperature NH_3-SCR catalysts with carbonate as precursors by ball milling method, RSC Adv. 12 (2022) 35094–35102, https://doi.org/10.1039/D2RA06552E.
[26] Z. Wei, D. Xiong, P. Duan, S. Ding, Y. Li, L. Li, P. Niu, X. Chen, Preparation of carbon-based solid acid catalysts using rice straw biomass and their application in hydration of α-Pinene, Catalysts 10 (2020) 213, https://doi.org/10.3390/catal10020213.
[27] N.S.M. Azlan, C.L. Yap, Y.W. Tiong, S. Gan, M.B.A. Rahman, The interplay of Brønsted-Lowry and lewis acid sites in bifunctional catalyst for the biomass conversion to levulinic acid, J. Biomim. Biomater. Biomed. Eng. 61 (2023) 71–76, https://doi.org/10.4028/p-RNTv04.
[28] X. Cheng, Y. Liu, K. Wang, H. Yu, S. Yu, S. Liu, High-Efficient conversion of cellulose to levulinic acid catalyzed via functional Brønsted–Lewis acidic ionic liquids, Catal. Lett. 152 (2022) 1064–1075, https://doi.org/10.1007/s10562-021-03701-w.
[29] Y. Han, L. Ye, X. Gu, P. Zhu, X. Lu, Lignin-based solid acid catalyst for the conversion of cellulose to levulinic acid using γ-valerolactone as solvent, Ind. Crop. Prod. 127 (2019) 88–93, https://doi.org/10.1016/j.indcrop.2018.10.058.
[30] Z. Chen, S. Zhang, B. Yan, Q. Cai, S. Zhang, Lignin-based solid acid catalyst for cellulose residue conversion into levulinic acid in biphasic system, Ind. Crop. Prod. 178 (2022) 369–379, https://doi.org/10.1016/j.indcrop.2022.114523.
[31] J. Fu, F. Yang, J. Mo, J. Zhuang, X. Lu, Catalytic decomposition of glucose to levulinic acid by synergy of organic Lewis acid and Brønsted acid in water, BioRes. 10 (2015) 1346–1356, https://doi.org/10.15376/biores.10.1.1346-1356.
[32] K. Shimizu, H. Furukawa, N. Kobayashi, Y. Itaya, A. Satsuma, Effects of Brønsted and Lewis acidities on activity and selectivity of heteropolyacid-based catalysts for hydrolysis of cellobiose and cellulose, Green. Chem. 11 (2009) 1627, https://doi.org/10.1039/b913737h.
[33] E.G.L. de Carvalho, F. de, A. Rodrigues, R.S. Monteiro, R.M. Ribas, M.J. da Silva, Experimental design and economic analysis of 5-hydroxymethylfurfural synthesis from fructose in acetone-water system using niobium phosphate as catalyst, Biomass. Convers. Biorefin. 8 (2018) 635–646, https://doi.org/10.1007/s13399-018-0319-5.
[34] R.S. de Carvalho, F. de A. Rodrigues, R.S. Monteiro, W.L. da Silva Faria, Optimization of furfural synthesis from xylose using niobic acid and niobium phosphate as catalysts, Waste Biomass. Valoriz. 10 (2019) 2673–2680, https://doi.org/10.1007/s12649-018-0272-3.
[35] X. Li, Y. Jiang, L. Wang, L. Meng, W. Wang, X. Mu, Effective low-temperature hydrolysis of cellulose catalyzed by concentrated $H_3PW_{12}O_{40}$ under microwave irradiation, RSC Adv. 2 (2012) 6921, https://doi.org/10.1039/c2ra21022c.
[36] N.S.M. Azlan, C.L. Yap, S. Gan, M.B.A. Rahman, Effectiveness of various solvents in the microwave-assisted extraction of cellulose from oil palm mesocarp fiber, Mater. Today Proc. 59 (2022) 583–590, https://doi.org/10.1016/J.MATPR.2021.12.086.
[37] N.S.M. Azlan, C.L. Yap, Y.W. Tiong, S. Gan, M.B.A. Rahman, Enhanced microwave conversion of oil palm mesocarp fiber to levulinic acid using $H_3PW_{12}O_{40}$-Nb_2O_5 functionalized carbon cryogel derived from lignin hydrogel, Bioresour. Technol. Rep. 25 (2024) 101750, https://doi.org/10.1016/j.biteb.2023.101750.
[38] M.M. Zainol, N.A.S. Amin, M. Asmadi, Synthesis and characterization of carbon cryogel microspheres from lignin–furfural mixtures for biodiesel production, Bioresour. Technol. 190 (2015) 44–50, https://doi.org/10.1016/j.biortech.2015.04.067.
[39] M. Schwan, S. Nefzger, B. Zoghi, C. Oligschleger, B. Milow, Improvement of solvent exchange for supercritical dried aerogels, Front. Mater. Sci. 8 (2021) 1–13, https://doi.org/10.3389/fmats.2021.662487.
[40] M.M. Zainol, N.A.S. Amin, M. Asmadi, Effects of thermal treatment on carbon cryogel preparation for catalytic esterification of levulinic acid to ethyl levulinate,

Fuel Process. Technol. 167 (2017) 431–441, https://doi.org/10.1016/j.fuproc.2017.07.028.
[41] W. Namchot, N. Panyacharay, W. Jonglertjunya, C. Sakdaronnarong, Hydrolysis of delignified sugarcane bagasse using hydrothermal technique catalyzed by carbonaceous acid catalysts, Fuel 116 (2014) 608–616, https://doi.org/10.1016/j.fuel.2013.08.062.
[42] E. Kolvari, N. Koukabi, M.M. Hosseini, Perlite: a cheap natural support for immobilization of sulfonic acid as a heterogeneous solid acid catalyst for the heterocyclic multicomponent reaction, J. Mol. Catal. A Chem. 397 (2015) 68–75, https://doi.org/10.1016/j.molcata.2014.10.026.
[43] Z. Sun, L. Xue, S. Wang, X. Wang, J. Shi, Single step conversion of cellulose to levulinic acid using temperature-responsive dodeca-aluminotungstic acid catalysts, Green. Chem. 18 (2016) 742–752, https://doi.org/10.1039/c5gc01730k.
[44] N.S.M. Azlan, C.L. Yap, Y.W. Tiong, S. Gan, M.B.A. Rahman, Sustainable biomass conversion to biofuel: recyclable nanoporous lignin-derived cryogel incorporated with $H_3PW_{12}O_{40}$–Nb_2O_5 for levulinic acid production, in: X. Wang (Ed.), Sustainable and Emerging Energy Technology, Springer, Cham, Switzerland, 2025.
[45] B.S. Rao, P.K. Kumari, D. Dhanalakshmi, N. Lingaiah, Selective conversion of furfuryl alcohol into butyl levulinate over zinc exchanged heteropoly tungstate supported on niobia catalysts, Mol. Catal. 427 (2017) 80–86, https://doi.org/10.1016/j.molcata.2016.11.032.
[46] Ch. Ramesh Kumar, P.S. Sai Prasad, N. Lingaiah, Aluminium exchanged heteropoly tungstate supported on titania catalysts: The generation of Lewis acidity and its role for benzylation reaction, J. Mol. Catal. A Chem. 350 (2011) 83–90, https://doi.org/10.1016/j.molcata.2011.09.011.
[47] P.K. Kumari, B.S. Rao, D. Dhana Lakshmi, N.R. Sai Paramesh, C. Sumana, N. Lingaiah, Tungstophosphoric acid supported on mesoporouus niobiumoxophosphate: an efficient solid acid catalyst for etherification of 5-hydroxymethylfurfural to 5-ethoxymethylfurfural, Catal. Today 325 (2019) 53–60, https://doi.org/10.1016/j.cattod.2018.06.047.
[48] Y. Zhang, J. Wang, J. Ren, X. Liu, X. Li, Y. Xia, G. Lu, Y. Wang, Mesoporous niobium phosphate: an excellent solid acid for the dehydration of fructose to 5-hydroxymethylfurfural in water, Catal. Sci. Technol. 2 (2012) 2485, https://doi.org/10.1039/c2cy20204b.
[49] M.N. Mohamad Ibrahim, N. Zakaria, C.S. Sipaut, O. Sulaiman, R. Hashim, Chemical and thermal properties of lignins from oil palm biomass as a substitute for phenol in a phenol formaldehyde resin production, Carbohydr. Polym. 86 (2011) 112–119, https://doi.org/10.1016/j.carbpol.2011.04.018.
[50] I.E. Raschip, G.E. Hitruc, C. Vasile, M.C. Popescu, Effect of the lignin type on the morphology and thermal properties of the xanthan/lignin hydrogels, Int. J. Biol. Macromol. 54 (2013) 230–237, https://doi.org/10.1016/J.IJBIOMAC.2012.12.036.
[51] F.A. Dawodu, O. Ayodele, J. Xin, S. Zhang, D. Yan, Effective conversion of non-edible oil with high free fatty acid into biodiesel by sulphonated carbon catalyst, Appl. Energy 114 (2014) 819–826, https://doi.org/10.1016/j.apenergy.2013.10.004.
[52] M. Hara, Biodiesel production by amorphous carbon bearing SO_3H, COOH and phenolic OH groups, a solid Brønsted acid catalyst, Top. Catal. 53 (2010) 805–810, https://doi.org/10.1007/s11244-010-9458-z.
[53] M.H.A. Elella, R.R. Mohamed, E.A. ElHafeez, M.W. Sabaa, Synthesis of novel biodegradable antibacterial grafted xanthan gum, Carbohydr. Polym. 173 (2017) 305–311, https://doi.org/10.1016/j.carbpol.2017.05.058.
[54] M.W. Sabaa, D.H. Hanna, M.H. Abu Elella, R.R. Mohamed, Encapsulation of bovine serum albumin within novel xanthan gum based hydrogel for protein delivery, Mater. Sci. Eng. C. 94 (2019) 1044–1055, https://doi.org/10.1016/j.msec.2018.10.040.
[55] T. Yamamoto, T. Sugimoto, T. Suzuki, S.R. Mukai, H. Tamon, Preparation and characterization of carbon cryogel microspheres, Carbon 40 (2002) 1345–1351, https://doi.org/10.1016/S0008-6223(01)00294-9.
[56] N.A.S. Ramli, N.A.S. Amin, Fe/HY zeolite as an effective catalyst for levulinic acid production from glucose: characterization and catalytic performance, Appl. Catal. B. 163 (2015) 487–498, https://doi.org/10.1016/j.apcatb.2014.08.031.
[57] Y. Liu, H. Li, J. He, W. Zhao, T. Yang, S. Yang, Catalytic conversion of carbohydrates to levulinic acid with mesoporous niobium-containing oxides, Catal. Commun. 93 (2017) 20–24, https://doi.org/10.1016/j.catcom.2017.01.023.
[58] X. Xu, B. Liang, Y. Zhu, J. Chen, T. Gan, H. Hu, Y. Zhang, Z. Huang, Y. Qin, Direct and efficient conversion of cellulose to levulinic acid catalyzed by carbon foam-supported heteropolyacid with Brønsted–Lewis dual-acidic sites, Bioresour. Technol. 387 (2023) 129600, https://doi.org/10.1016/j.biortech.2023.129600.
[59] J.S. Kruger, V. Nikolakis, D.G. Vlachos, Carbohydrate dehydration using porous catalysts, Curr. Opin. Chem. Eng. 1 (2012) 312–320, https://doi.org/10.1016/j.coche.2012.06.003.
[60] W. Zeng, D. Cheng, H. Zhang, F. Chen, X. Zhan, Dehydration of glucose to levulinic acid over MFI-type zeolite in subcritical water at moderate conditions, React. Kinet. Mech. Catal. 100 (2010) 377–384, https://doi.org/10.1007/s11144-010-0187-x.
[61] N. Ya'aini, N.A.S. Amin, S. Endud, Characterization and performance of hybrid catalysts for levulinic acid production from glucose, Microporous Mesoporous Mater. 171 (2013) 14–23, https://doi.org/10.1016/j.micromeso.2013.01.002.
[62] D. Verboekend, J. Pérez-Ramírez, Design of hierarchical zeolite catalysts by desilication, Catal. Sci. Technol. 1 (2011) 879, https://doi.org/10.1039/c1cy00150g.
[63] F. Thibault-Starzyk, I. Stan, S. Abelló, A. Bonilla, K. Thomas, C. Fernandez, J.-P. Gilson, J. Pérez-Ramírez, Quantification of enhanced acid site accessibility in hierarchical zeolites – the accessibility index, J. Catal. 264 (2009) 11–14, https://doi.org/10.1016/j.jcat.2009.03.006.
[64] S. Brunauer, L.S. Deming, W.E. Deming, E. Teller, On a theory of the van der waals adsorption of gases, J. Am. Chem. Soc. 62 (1940) 1723–1732, https://doi.org/10.1021/ja01864a025.
[65] M. Thommes, K. Kaneko, A.V. Neimark, J.P. Olivier, F. Rodriguez-Reinoso, J. Rouquerol, K.S.W. Sing, Physisorption of gases, with special reference to the evaluation of surface area and pore size distribution (IUPAC Technical Report), Pure Appl. Chem. 87 (2015) 1051–1069, https://doi.org/10.1515/pac-2014-1117.
[66] P. Pang, H. Han, L. Hu, C. Guo, Y. Gao, Y. Xie, The calculations of pore structure parameters from gas adsorption experiments of shales: which models are better? J. Nat. Gas. Sci. Eng. 94 (2021) 104060 https://doi.org/10.1016/j.jngse.2021.104060.
[67] Z.Y. Zakaria, J. Linnekoski, N.A.S. Amin, Catalyst screening for conversion of glycerol to light olefins, Chem. Eng. J. 207–208 (2012) 803–813, https://doi.org/10.1016/j.cej.2012.07.072.
[68] K. Wang, J. Jiang, X. Liang, H. Wu, J. Xu, Direct conversion of cellulose to levulinic acid over multifunctional sulfonated humins in Sulfolane–Water solution, ACS Sustain. Chem. Eng. 6 (2018) 15092–15099, https://doi.org/10.1021/acssuschemeng.8b03558.
[69] H.E. van der Bij, B.M. Weckhuysen, Phosphorus promotion and poisoning in zeolite-based materials: synthesis, characterisation and catalysis, Chem. Soc. Rev. 44 (2015) 7406–7428, https://doi.org/10.1039/C5CS00109A.
[70] N. Katada, T. Tsubaki, M. Niwa, Measurements of number and strength distribution of Brønsted and Lewis acid sites on sulfated zirconia by ammonia IRMS–TPD method, Appl. Catal. A Gen. 340 (2008) 76–86, https://doi.org/10.1016/j.apcata.2008.01.033.
[71] H. Mochizuki, T. Yokoi, H. Imai, S. Namba, J.N. Kondo, T. Tatsumi, Effect of desilication of H-ZSM-5 by alkali treatment on catalytic performance in hexane cracking, Appl. Catal. A Gen. 449 (2012) 188–197, https://doi.org/10.1016/j.apcata.2012.10.003.
[72] K. Lu, Y. Wang, L. Zhu, B. Xing, S. Wang, Efficient conversion of biomass-derived saccharides to levulinic acid using silicotungstic acid, Energy Fuels 37 (2023) 6642–6650, https://doi.org/10.1021/acs.energyfuels.3c00948.
[73] S. Hu, F. Jiang, Y.Lo Hsieh, 1D lignin-based solid acid catalysts for cellulose hydrolysis to glucose and nanocellulose, ACS Sustain. Chem. Eng. 3 (2015) 2566–2574, https://doi.org/10.1021/acssuschemeng.5b00780.
[74] M.M. Zainol, N.A.S. Amin, M. Asmadi, Synthesis and characterization of porous microspherical ionic liquid carbon cryogel catalyst for ethyl levulinate production, Diam. Relat. Mater. 95 (2019) 154–165, https://doi.org/10.1016/j.diamond.2019.04.014.
[75] A. Zhu, Q. Li, L. Li, J. Wang, One-pot synthesis of 3,4-dihydro-2(H)-pyrimidinones catalyzed by reusable acidic choline-based ionic liquids, Catal. Lett. 143 (2013) 463–468, https://doi.org/10.1007/s10562-013-0978-6.
[76] T. Kitano, T. Shishido, K. Teramura, T. Tanaka, Brønsted acid property of alumina-supported niobium oxide calcined at high temperatures: Characterization by acid-catalyzed reactions and spectroscopic methods, J. Phys. Chem. C. 116 (2012) 11615–11625, https://doi.org/10.1021/jp3032429.
[77] Z. Zhang, Z. Li, H. Zhang, C. Ma, Z. Zhang, Y. Xie, S. Liu, Q. Wang, C.U. Pittman, Selective catalytic conversion of kraft lignin into monoaromatic hydrocarbons over niobium oxide catalysts, Fuel Process. Technol. 235 (2022) 107832, https://doi.org/10.1016/j.fuproc.2022.107382.